Geosci. Model Dev. Discuss., 8, 5367–5418, 2015
www.geosci-model-dev-discuss.net/8/5367/2015/
doi:10.5194/gmdd-8-5367-2015


Geoscientific Model Development Discussions



# Simulation of atmospheric $N_2O$ with GEOS-Chem and its adjoint: evaluation of observational constraints

**K. C. Wells[1], D. B. Millet[1], N. Bousserez[2], D. K. Henze[2], S. Chaliyakunnel[1], T. J. Griffis[1], Y. Luan[1], E. J. Dlugokencky[3], R. G. Prinn[4], S. O'Doherty[5], R. F. Weiss[6], G. S. Dutton[3,7], J. W. Elkins[3], P. B. Krummel[8], R. Langenfelds[8], L. P. Steele[8], E. A. Kort[9], S. C. Wofsy[10], and T. Umezawa[11,12]**

[1]Department of Soil, Water, and Climate, University of Minnesota, St. Paul, Minnesota, USA
[2]Department of Mechanical Engineering, University of Colorado at Boulder, Boulder, Colorado, USA
[3]Earth System Research Laboratory, NOAA, Boulder, Colorado, USA
[4]Center for Global Change Science, Massachusetts Institute of Technology, Cambridge, Massachusetts, USA
[5]School of Chemistry, University of Bristol, Bristol, UK
[6]Scripps Institute of Oceanography, University of California, San Diego, La Jolla, California, USA
[7]CIRES, University of Colorado, Boulder, Colorado, USA
[8]CSIRO Oceans and Atmosphere Flagship, Aspendale, Victoria, Australia







[9]Department of Atmospheric, Oceanic, and Space Sciences, University of Michigan, Ann Arbor, Michigan, USA
[10]School of Engineering and Applied Science and Department of Earth and Planetary Sciences, Harvard University, Cambridge, Massachusetts, USA
[11]Center for Atmospheric and Oceanic Studies, Tohoku University, Sendai, Japan
[12]Max-Planck Institute for Chemistry, Mainz, Germany

Received: 27 May 2015 – Accepted: 09 June 2015 – Published: 08 July 2015

Correspondence to: D. B. Millet (dbm@umn.edu)

Published by Copernicus Publications on behalf of the European Geosciences Union.





GMDD
8, 5367–5418, 2015



## Abstract

We describe a new 4D-Var inversion framework for $N_2O$ based on the GEOS-Chem chemical transport model and its adjoint, and apply this framework in a series of observing system simulation experiments to assess how well $N_2O$ sources and sinks can be constrained by the current global observing network. The employed measurement ensemble includes approximately weekly and quasi-continuous $N_2O$ measurements (hourly averages used) from several long-term monitoring networks, $N_2O$ measurements collected from discrete air samples aboard a commercial aircraft (CARIBIC), and quasi-continuous measurements from an airborne pole-to-pole sampling campaign (HIPPO). For a two-year inversion, we find that the surface and HIPPO observations can accurately resolve a uniform bias in emissions during the first year; CARIBIC data provide a somewhat weaker constraint. Variable emission errors are much more difficult to resolve given the long lifetime of $N_2O$, and major parts of the world lack significant constraints on the seasonal cycle of fluxes. Current observations can largely correct a global bias in the stratospheric sink of $N_2O$ if emissions are known, but do not provide information on the temporal and spatial distribution of the sink. However, for the more realistic scenario where source and sink are both uncertain, we find that simultaneously optimizing both would require unrealistically small errors in model transport. Regardless, a bias in the magnitude of the $N_2O$ sink would not affect the a posteriori $N_2O$ emissions for the two-year timescale used here, given realistic initial conditions, due to the timescale required for stratosphere–troposphere exchange (STE). The same does not apply to model errors in the rate of STE itself, which we show exerts a larger influence on the tropospheric burden of $N_2O$ than does the chemical loss rate over short ($< 3$ year) timescales. We use a stochastic estimate of the inverse Hessian for the inversion to evaluate the spatial resolution of emission constraints provided by the observations, and find that significant, spatially explicit constraints can be achieved in locations near and immediately upwind of surface measurements and the HIPPO flight tracks; however, these are mostly confined to North America, Europe, and Australia.





GMDD
8, 5367–5418, 2015



None of the current observing networks are able to provide significant spatial information on tropical $N_2O$ emissions. There, averaging kernels are highly smeared spatially and extend even to the midlatitudes, so that tropical emissions risk being conflated with those elsewhere. For global inversions, therefore, the current lack of constraints on the tropics also places an important limit on our ability to understand extratropical emissions. Based on the error reduction statistics from the inverse Hessian, we characterize the atmospheric distribution of unconstrained $N_2O$, and identify regions in and downwind of South America, Central Africa, and Southeast Asia where new surface or profile measurements would have the most value for reducing present uncertainty in the global $N_2O$ budget.

## 1 Introduction

Nitrous oxide ($N_2O$) is a long-lived greenhouse gas with a global warming potential approximately 300 times that of $CO_2$ on a 100 year timescale (Forster et al., 2007). It is a key player in stratospheric chemistry; $N_2O$ emissions weighted by their ozone depletion potential currently outrank any other substance (Ravishankara et al., 2009). $N_2O$ is produced via microbial nitrification and denitrification reactions in soils (Firestone and Davidson, 1989) and ocean waters (Elkins et al., 1978; Cohen and Gordon, 1979; Law and Owens, 1990), with soils contributing the majority of the global flux (Mosier et al., 1998). Agricultural activities such as fertilizer application and animal waste management enhance these nitrification and denitrification reactions (Maggiotto et al., 2000), leading to direct on-site emissions as well as indirect emissions downstream due to leaching and runoff (IPCC, 2006). Energy production and transportation (Denman et al., 2007) and biomass burning emissions (van der Werf et al., 2010) also contribute to the global $N_2O$ source. $N_2O$ is lost in the stratosphere via photolysis and reaction with $O(^1D)$, leading to a global lifetime currently estimated at ∼ 122–131 years (Volk et al., 1997; Prather et al., 2012). Atmospheric $N_2O$ is currently increasing at ∼ 0.8 ppb $yr^{-1}$ (http://ds.data.jma.go.jp/gmd/wdcgg/pub/global/globalmean.html),





GMDD
8, 5367–5418, 2015



driven by accelerating human perturbation of the nitrogen cycle: in particular, rising application of nitrogen fertilizers (Galloway et al., 2008; Davidson, 2009; Park et al., 2012) and the nonlinear response of soil $N_2O$ emissions to fertilizer inputs in excess of crop demands (Shcherbak et al., 2014).

Rates of microbial nitrification and denitrification in soils depend strongly on environmental characteristics such as temperature (Potter et al., 1996), moisture (Bouwman, 1998; Bouwman et al., 2013) and the make-up of the soil microbial community (Butterbach-Bahl et al., 2013), and as a result large uncertainties exist in the spatial and temporal distribution of global $N_2O$ emissions. Long-term flask-based and in-situ observations of atmospheric $N_2O$ are available from a number of monitoring networks around the world, along with routine and intensive aircraft observations, and there have been several recent studies employing these data to generate top-down estimates of global $N_2O$ emissions. Huang et al. (2008) derived a global $N_2O$ flux of 14.1–17.1 $\mathrm{Tg\,N\,yr^{-1}}$ for 2002–2005 using surface observations from four different surface monitoring networks. Based on aircraft observations from the first two HIAPER Pole-to-Pole Observations (HIPPO) campaigns, Kort et al. (2011) found evidence for large and episodic tropical fluxes. Saikawa et al. (2014) combined surface observations with aircraft- and ship-based measurements to derive regional $N_2O$ emission estimates for five source sectors, and inferred a global flux of $18.1 \pm 0.6\,\mathrm{Tg\,N\,yr^{-1}}$ for 2002–2005. Thompson et al. (2014a) used ground- and ship-based observations to estimate regional $N_2O$ emissions and their interannual variability. Their study yielded global fluxes for 1999–2009 that ranged from 17.5 to 20.1 $\mathrm{Tg\,N\,yr^{-1}}$, with interannual variability driven largely by fluctuations in tropical and subtropical soil fluxes. A recent intercomparison of top-down inversion results using different transport models gave a comparable range of global fluxes: 16.1–18.7 $\mathrm{Tg\,N\,yr^{-1}}$ for 2006–2009 (Thompson et al., 2014c).

Some previous work has found that uncertainties in stratosphere–troposphere exchange (STE) and the associated influx of $N_2O$-depleted air can give rise to significant uncertainties in $N_2O$ source inversions, depending on the time range and scale on which the emissions are optimized (Nevison et al., 2005; Hirsch et al., 2006; Huang





GMDD
8, 5367–5418, 2015



et al., 2008). On the other hand, Thompson et al. (2011) found their a posteriori surface fluxes to be quite insensitive to biases in the $N_2O$ stratospheric loss rate during the first year of a multi-year simulation. They also found that combining surface and aircraft observations could provide some constraint on the magnitude of the stratospheric $N_2O$ sink in a simultaneous source-sink inversion, without increasing errors in the a posteriori $N_2O$ emissions. However, biases in the model STE itself did give rise to regional uncertainties of up to 25 % in the optimized source.

The global observing network for atmospheric $N_2O$ includes flask-based measurements and quasi-continuous in-situ instruments, as well as both surface- and airborne sampling platforms. However, a full quantification of the relative utility of these different datasets has not yet been performed. Such information is needed in order to determine: (i) the degree to which current observations can be used to constrain $N_2O$ emissions and stratospheric loss, and the comparative value of different observing strategies for doing so; (ii) the spatial and temporal resolution at which $N_2O$ sources and sinks can be constrained by these different datasets; and (iii) where additional measurements are most needed to advance present understanding of the atmospheric $N_2O$ budget.

In this paper, we introduce a new simulation and inversion framework for atmospheric $N_2O$ using the GEOS-Chem chemical transport model (CTM) and its adjoint. The adjoint-based variational method is advantageous as it allows us to solve for $N_2O$ fluxes at the spatial resolution of the CTM and at any desired time step, thus minimizing any impact from aggregation errors. Here, we apply the model in a simulation environment (i.e., in observing system simulation experiments, or OSSEs) to quantify the $N_2O$ source and sink constraints provided by: (i) flask and quasi-continuous surface observations from a number of long-term monitoring networks, (ii) routine flask observations from an instrument platform deployed aboard a commercial aircraft (CARIBIC), and (iii) in situ airborne observations made during a series of intensive pole-to-pole field campaigns (HIPPO). This is the first study to quantify the individual constraints provided by these different observation ensembles. We determine the potential for model errors in the stratospheric loss rate of $N_2O$ to bias the inferred emission estimates, and assess





GMDD
8, 5367–5418, 2015



how well $N_2O$ emissions and stratospheric loss can be simultaneously constrained by the above observations. We evaluate the temporal and spatial resolution of emission constraints afforded by the different $N_2O$ observations, and explore the impact of uncertainties in the a priori error estimates on the inferred fluxes. Finally, we apply the above information to identify regions that are underconstrained by the current $N_2O$ observing network, and the downwind locations where new measurements would be most valuable for reducing current uncertainty in the $N_2O$ budget.

## 2 $N_2O$ simulation in the GEOS-Chem CTM

In this work we implement an $N_2O$ simulation in the GEOS-Chem (http://www.geos-chem.org) global 3-D model of atmospheric chemistry. Analyses presented here use GEOS-5 assimilated meteorological data from the NASA Goddard Earth Observing System, degraded to a horizontal resolution of $4^\circ \times 5^\circ$ and to a vertical grid containing 47 levels from the surface to 0.01 hPa. Transport is calculated on a 30 min time step; a 60 min time step is used for emissions and chemistry. Our simulation period runs from April 2010 to April 2012.

A priori $N_2O$ emissions are grouped into four categories: anthropogenic sources (including industrial processes, transportation, residential/waste management, and agricultural activities), natural soil fluxes, biomass burning, and oceanic exchange. Annual emissions for anthropogenic activities are obtained from the Emission Database for Global Atmospheric Research (EDGARv4.2, http://edgar.jrc.ec.europa.eu). Within this database there are 12 emission sectors as defined by the IPCC (IPCC, 2006). These sectors are listed in Table 1, along with the corresponding total emissions for 2008. The overall anthropogenic $N_2O$ flux from EDGARv4.2 is 6.9 Tg N $yr^{-1}$, with 2.4 Tg N $yr^{-1}$ from industrial and residential sources and 4.5 Tg N $yr^{-1}$ from direct and indirect agricultural emissions. Natural soil emissions of $N_2O$ are computed based on the EDGARv2 database, which provides an annual flux at $1^\circ \times 1^\circ$ resolution for the year 1990 totaling 3.2 Tg N $yr^{-1}$. Biomass burning emissions of $N_2O$ are prescribed monthly based on





GMDD
8, 5367–5418, 2015



the Global Fire Emissions Database version 3 (GFEDv3, van der Werf et al., 2010) and total 0.6 Tg N $yr^{-1}$ for 2010–2011. Thermal and biogeochemical oceanic fluxes of $N_2O$ are calculated monthly at 4.5° × 3.75° following Jin and Gruber (2003), leading to a net annual global source of 3.5 Tg N $yr^{-1}$. Figure 1 maps the resulting annual flux from soils, anthropogenic activities, biomass burning, and air–sea exchange, with a cumulative annual global source of 14.2 Tg N $yr^{-1}$. We note that this is below the range of current top-down flux estimates (~ 16 to 20 Tg N $yr^{-1}$) discussed previously.

Stratospheric destruction of $N_2O$ is calculated using archived monthly 3-D loss frequencies from Global Modeling Initiative (GMI) simulations driven by MERRA meteorological fields (MERRA is also based on GEOS-5). The resulting stratospheric loss gives rise to a 127.5 year lifetime, which is in the range of current estimates (122–131 years, Volk et al., 1997; Prather et al., 2012). This lifetime depends upon the initial mass distribution assumed for $N_2O$, which we describe below.

Because of the long atmospheric lifetime of $N_2O$, generating realistic initial conditions is of critical importance for top-down analyses of its sources and sinks. Some previous studies have included initial conditions as part of the state vector for optimization, or prescribed $N_2O$ mass fields from simulations that have reached a pseudo-steady state. We instead construct an initial 3-D $N_2O$ field using global observations for March 2010 (Fig. 2), one month prior to the start of our optimization window. This timing is chosen to accommodate a brief model spin-up that smooths any artificial horizontal gradients prescribed in the initial conditions. Initial tropospheric concentrations are computed from NOAA Carbon Cycle and Greenhouse Gases (CCGG) flask observations (described below) averaged monthly and zonally at 4° resolution. These mixing ratios are then assumed uniform from the surface to the tropopause. Above 100 hPa, our initial conditions are based on monthly mean (March 2010) $N_2O$ profiles measured by the Microwave Limb Sounder (MLS) onboard the EOS Aura satellite (Lambert et al., 2007) interpolated onto the GEOS-Chem horizontal and vertical grid. Where needed, we then perform a linear interpolation between the tropopause and 100 hPa.





GMDD
8, 5367–5418, 2015



## 3 Inversion set-up and verification

We use a 4D-Var inversion framework to solve for spatially resolved, monthly $N_2O$ fluxes based on the atmospheric measurements described next (Sect. 4). Optimal fluxes are derived by minimizing the cost function, $J(\boldsymbol{p})$, which contains contributions from the error weighted model-measurement differences and a penalty term:

$$J(\boldsymbol{p}) = \frac{1}{2}\sum_{c\in\Omega}(\boldsymbol{c}-\boldsymbol{y})^T\mathbf{S}_y^{-1}(\boldsymbol{c}-\boldsymbol{y}) + \frac{1}{2}\gamma(\boldsymbol{p}-\boldsymbol{p}_a)^T\mathbf{S}_a^{-1}(\boldsymbol{p}-\boldsymbol{p}_a) \quad (1)$$

Here, $\boldsymbol{p}$ is the vector of parameters to be optimized, $\boldsymbol{p}_a$ is the initial (a priori) value of those parameters, $\boldsymbol{y}$ is a set of observations, $\boldsymbol{c}$ is a vector containing the model-simulated concentrations, $\mathbf{S}_y$ and $\mathbf{S}_a$ are the observational and a priori emissions error covariance matrices, respectively, $\Omega$ is the time and space domain of the observations, and $\gamma$ is a regularization parameter (set here to 1.0).

In this study, $\boldsymbol{p}$ contains monthly scaling factors for the terrestrial and oceanic emissions of $N_2O$ and for stratospheric loss frequencies. The adjoint model calculates the gradient of the cost function with respect to this state vector, $\nabla_p J(\boldsymbol{p})$, and employs a quasi-Newton minimization routine to iteratively minimize $J(\boldsymbol{p})$ (Zhu et al., 1994; Byrd et al., 1995). Scale factors for emissions are optimized on the $4^\circ \times 5^\circ$ GEOS-Chem grid, while those for the stratospheric loss frequencies are aggregated over the vertical extent of the stratosphere and into eight latitude bands of $22.5^\circ$. This results in a state vector with 79 488 elements for emissions and 192 elements for stratospheric loss. We use a lower bound of zero in the optimization routine to avoid a solution containing negative scaling factors and an upper bound of 10 that was found to improve optimization performance. Use of the lower bound corresponds to an implicit assumption that ocean regions with net $N_2O$ uptake are no stronger of a sink than in the prior, while the upper bound corresponds to an assumption that the a priori emissions are not biased low by more than a factor of 10. These assumptions are not problematic for the synthetic experiments presented here, but could be when performing real inversions.





GMDD
8, 5367–5418, 2015



We assume 100 % uncertainty in the a priori emissions (for any given grid square and month) and in the stratospheric loss frequencies and impose horizontal correlation length scales for emissions of 500 km over land and 1000 km over ocean, following Thompson et al. (2011, 2014a). The observational error covariance matrix contains contributions from the measurement uncertainty (typically 0.4 ppb, see next section for details) and from model transport errors. We estimate the latter from the variance in modeled $N_2O$ mixing ratios across all grid boxes adjacent to that containing a given observation.

The adjoint modules for optimizing $N_2O$ emissions and stratospheric loss were verified by comparing adjoint and finite difference sensitivities calculated for each atmospheric column with no horizontal transport. We find good agreement between adjoint and finite difference sensitivities for both emissions and stratospheric loss scaling factors (Fig. S1), demonstrating the accuracy of the $N_2O$ adjoint code. Propagation of adjoint sensitivities through horizontal transport in the GEOS-Chem adjoint has been verified previously (Henze et al., 2007). The GEOS-Chem adjoint has been used for a wide range of research applications such as constraining sources of aerosols (Henze et al., 2007, 2009; Kopacz et al., 2011; Wang et al., 2012; Xu et al., 2013), CO (Kopacz et al., 2009, 2010), $NH_3$ (Zhu et al., 2013), $O_3$ (Zhang et al., 2009; Parrington et al., 2012), and methanol (Wells et al., 2014), and to assess the impact of different types of observations on CO source inversions (Jiang et al., 2011, 2013).

## 4 Global observations of atmospheric $N_2O$

Below, we apply GEOS-Chem and its adjoint to assess the $N_2O$ source and sink constraints provided by the current suite of global observations. We include in this assessment several long-term surface monitoring networks and two aircraft platforms. A full list of the surface observation sites can be found in Table 2, and their locations are mapped in Fig. 3. The majority of the surface observations are from discrete air samples collected approximately weekly in flasks at 77 sites in the NOAA CCGG program





GMDD
8, 5367–5418, 2015



(Dlugokencky et al., 1994), which are analyzed using a gas chromatograph with an electron capture detector and reported on the NOAA 2006A calibration scale. We also use flask measurements from six sites in the Commonwealth Scientific and Industrial Research Organisation (CSIRO) network (also on the NOAA 2006A scale; Francey et al., 1996; Cooper et al., 1999), five sites in the Environment Canada (EC) network (NOAA 2006 scale), and one National Institute of Water and Atmospheric research (NIWA) site (NOAA 2006A scale). We assume a measurement uncertainty of 0.4 ppb for all of the above flask measurements, based on recommendations from the data providers. Hourly averages of quasi-continuous measurements are employed from six sites in the NOAA Chromatograph for Atmospheric Trace Species (CATS) network, six sites in the Advanced Global Atmospheric Gases Experiment (AGAGE) network (Prinn et al., 2000), and the University of Minnesota tall tower Trace Gas Observatory (KCMP tall tower) site (Griffis et al., 2013). Measurements from the AGAGE network are reported on the SIO-98 scale, and have a reported uncertainty of 0.2 % (0.6 ppb). Measurements at the KCMP tall tower and those in the CATS network (both on the NOAA 2006A scale) have uncertainties of about 1.0 and 0.3 ppb, respectively.

Extensive airborne measurements of $N_2O$ are available from the Civil Aircraft for the Regular Investigation of the atmosphere Based on an Instrument Container (CARIBIC) observatory (Brenninkmeijer et al., 2007). CARIBIC provides flask measurements from a commercial Lufthansa aircraft, with data available for 79 flights between Frankfurt, Germany and a number of other cities around the world (Fig. 3) during the time period of our optimization. These observations have an uncertainty of about 0.35 ppb and are reported on the NOAA 2006 scale (Schuck et al., 2009). Since the CARIBIC observatory is operated on a passenger aircraft, the majority of measurements are taken at a cruising altitude of 9–12 km: about 50 % (in general those at higher latitudes, depending on synoptic conditions) are in the lowermost stratosphere, with the remainder sampling the upper troposphere (Assonov et al., 2013; Umezawa et al., 2014).

High-frequency airborne $N_2O$ measurements were made by quantum cascade laser spectroscopy (QCLS) during the HIAPER Pole-to-Pole Observations (HIPPO) cam-





GMDD
8, 5367–5418, 2015



paigns (Wofsy, 2011; flight tracks mapped in Fig. 3). Three of the five HIPPO deployments took place during our optimization window: HIPPO III (24 March–16 April 2010), HIPPO IV (14 June–11 July 2011), and HIPPO V (9 August–9 September 2011), totaling 33 flights over the April 2010–April 2012 time frame. Measurements are reported on the NOAA 2006 scale (Kort et al., 2011). The HIPPO flights range from pole-to-pole while profiling the atmosphere from the surface to the tropopause at regular intervals. Unlike the other available datasets, which provide recurrent measurements at discrete locations or along specific flight paths, the HIPPO datasets provide ∼ 1 month global cross-sections of atmospheric concentration.

The use of different calibration scales results in offsets between different networks measuring $N_2O$, which may also vary with time. Because variability in atmospheric $N_2O$ is low, these offsets can have a significant impact on the a posteriori solution. As the results presented here involve synthetic observations at the time and location of the real observations, we do not consider the impact of these offsets on inferred $N_2O$ emissions and stratospheric loss. However, for inversions employing real $N_2O$ measurements, we calculate offsets at collocated sites to adjust those measurements that are not reported on the NOAA 2006A scale.

## 5 Evaluating constraints on $N_2O$ emissions and stratospheric loss using pseudo observations

In this section we perform a range of pseudo observation tests to determine how well $N_2O$ sources (and sinks) can be quantified, and at what space–time resolution, based on the observing network described above. In these tests, we sample the model at the time and location of each observation to generate pseudo observations. We then perform a two-year inversion in which we assimilate pseudo observations generated for the surface network, CARIBIC flights, or HIPPO flights, or for a combination of those datasets. Our state vector contains monthly scaling factors for emissions, stratospheric loss frequencies, or both. We start with a spatially-uniform incorrect a priori value for





GMDD
8, 5367–5418, 2015



these scaling factors; the degree to which the optimization converges to the true value of 1.0 for each grid cell and month gives a measure of the ability of the observations to correct for model biases in these processes. A full list of all pseudo observation tests performed is given in Table 3.

### 5.1 Constraints on $N_2O$ emissions

Figure 4 shows the results of synthetic inversions in which we optimize emissions based on surface-based pseudo observations as described above. Here we impose a time invariant a priori emission bias of ±50 % across all land and ocean grid cells, while keeping the stratospheric loss rates fixed at their true model values. We see that for the first ~ 20 months of the optimization window, the surface-based inversion is able to correct the imposed bias over most land and ocean regions that have a significant flux. However we will show later that this does not mean current observations can fully constrain the spatial distribution of $N_2O$ emissions at the $4^\circ \times 5^\circ$ resolution shown in Fig. 4.

Overall, the solution is of comparable quality whether we start with a high or low a priori bias, with some minor distinctions: the test with the positive initial bias performs slightly better over oceans and in later months of the simulation, and also converges more quickly (5 iterations vs. 10 for the test with a low initial bias). However, the situation is very different when no upper bound is imposed on the solution. In this case, when given a low initial bias the optimization tends to overshoot the truth in high-flux regions while underestimating the truth in low-flux regions. Imposing both lower and upper bounds on the inverse solution (in this case, 0 and 10) is thus important to ensure a consistent solution across high and low initial bias scenarios. Jiang et al. (2014) concluded that construction of the a priori constraint was the most important factor affecting the consistency of solutions for divergent initial assumptions in the case of CO; we find here that the prior bounds placed on the solution can have a comparable impact for $N_2O$.





GMDD
8, 5367–5418, 2015



Figure 4 also indicates that during the last several months of the optimization window there is inadequate forcing for the inversion to completely correct for the initial emission biases, particularly over the Southern Hemisphere. This is largely due to the timescale required to transport $N_2O$ between source regions and receptor locations – in the Southern Hemisphere observing stations are sparse and distant from major $N_2O$ sources. As a result, there are relatively few subsequent observations that are influenced by biases imposed towards the end of the optimization window.

Figure 5 shows zonally integrated, annual a posteriori emissions from synthetic inversions using surface, CARIBIC, or HIPPO pseudo observations. In each case the state vector for optimization includes monthly emission scale factors on the model grid (but not stratospheric loss rates), and an initial bias of ±50 % is applied to emissions in all grid boxes. Results are shown only for the first year of the optimization period since (as shown) the inversion has less ability to retrieve the true emissions in the succeeding months; there are also no HIPPO observations during the last six months of the simulation. As discussed, the surface data provide a good correction to the imposed prior error in $N_2O$ emissions when starting with both high and low initial biases, and can accurately retrieve zonally integrated emissions in the Northern and Southern Hemispheres.

We see in Fig. 5 that inversions based on the HIPPO data are also able to capture the zonal distribution of $N_2O$ emissions. For the high-bias test (a priori emissions scaling factor of 1.5), the inversion results are very similar to those obtained using the surface data. For the low-bias test, the a posteriori emissions retain a low bias over the Southern Ocean, and overshoot slightly where emissions peak in both hemispheres. On the other hand, the CARIBIC measurements lead to substantially different a posteriori fluxes between the high- and low-bias tests: the inversion with the high initial bias returns the true zonal distribution of emissions quite well, whereas the test with the low initial bias leads to an overestimate of emissions from 20–30° N and an underestimate elsewhere. We find through these tests that each dataset can independently resolve the global annual flux to within 5 % of the true value (Table 3).





GMDD
8, 5367–5418, 2015



Based on these experiments, we conclude that relatively sparse observations in the upper troposphere and lowermost stratosphere such as those from CARIBIC are sufficient to correct a prior bias in the global annual $N_2O$ emissions, but do not provide as robust a constraint on the zonal distribution of those emissions. The pole-to-pole HIPPO observations provide a stronger constraint on the zonal distribution of annual emissions despite the fact that they do not cover the full time period of our optimization. This is because the long lifetime of $N_2O$ allows emissions perturbations to impact concentrations far from source regions 2–6 months after the perturbation (Thompson et al., 2014a). Of the three networks examined here (surface, CARIBIC, and HIPPO) in isolation, the regular surface measurements provide the best correction of annual emission biases.

The above OSSEs were performed based on an initial fractional emission bias that is uniform in space and time (i.e., prior emissions set everywhere to 0.5× or 1.5× the true model values). As we will see later, emission biases that vary in space or time are much more difficult to resolve, due to the sparse observing network combined with the long atmospheric lifetime of $N_2O$.

### 5.2 Stratospheric loss of $N_2O$: constraints from the observing network and impact on source inversions

An important finding from previous work is that $N_2O$ emission estimates derived from surface concentration measurements can be biased by model errors in the stratospheric sink of $N_2O$ (Thompson et al., 2011). Here, we explore the potential for the airborne observations provided by CARIBIC and HIPPO, in conjunction with the surface network, to simultaneously constrain $N_2O$ sources as well as sinks. To this end, we perform a series of synthetic inversions with a prior bias imposed on the stratospheric loss frequencies for $N_2O$ (aggregated to eight equal latitude bands), and assess the degree to which we can correct for errors in the $N_2O$ sink (given a fixed $N_2O$ source) or both the source and sink of $N_2O$ (simultaneously). As previously, a prior scaling factor





GMDD
8, 5367–5418, 2015



of either 0.5 or 1.5 is applied to each location and month, and we attempt to retrieve the true value of 1.0 in each case.

Figure 6 shows the resulting a posteriori scaling factors for stratospheric loss frequencies when $N_2O$ emissions are held fixed (and equal to their "true" values). We can see that each observational dataset provides some information to correct for biases in the loss frequencies in the first year of the simulation. Stratospheric loss of $N_2O$ in the second (i.e. final) year of the inversion does not significantly affect the observations, given a characteristic timescale for stratosphere-to-troposphere mixing of 1–2 years (Salstein, 1995); as a result, the corresponding a posteriori scale factors do not diverge significantly from their prior values.

For the inversion using surface data, the optimized annual global sink in the first year of the simulation is very close to the true value (Table 3), but the loss frequencies are only adjusted throughout the first year in the tropics. In the extratropics, they adjust primarily during the summer months. The extratropical timing corresponds to the observed seasonal minimum of $N_2O$ at these latitudes (Nevison et al., 2011). At their peaks, retrieved values in the Southern Hemisphere approach the truth, whereas in the Northern Hemisphere they slightly overshoot the true sink. A posteriori values near the poles remain close to the a priori in both hemispheres. Solutions achieved using HIPPO or CARIBIC data are spatially similar to those obtained with the surface observations, although the optimized global sink for both is biased low (by 13–17 %, Table 3) due to weaker forcing (fewer total observations, higher observation uncertainty). Therefore, while all the observations provide some correction of biases in the global stratospheric sink of $N_2O$ given known surface fluxes (with the surface data providing the strongest constraint), they provide limited information on the spatial and temporal distribution of that sink.

Also shown in Fig. 6 are the a posteriori scaling factors for stratospheric loss frequencies of $N_2O$ when both the source and sink are optimized simultaneously, and given an initial 50 % low bias for each. In these tests, the sink does not return to the true value (Table 3); for the inversions using CARIBIC and HIPPO it actually moves in





GMDD
8, 5367–5418, 2015



the opposite direction (i.e. further from the truth than the a priori) due to the forcing imposed by the source bias. In other words, the inversion is not able to resolve a bias in $N_2O$ emissions from a bias in the sink. Despite this behavior, the spatial distribution of the derived scaling factors for $N_2O$ emissions (not shown) closely matches that obtained with a fixed ("true") stratospheric sink, and the annual a posteriori emission flux is within 5 % of the truth (Table 3) for all tests except the high-bias test using CARIBIC pseudo-data. Therefore, on the 1–2 year timescale of our optimization, and given accurate initial conditions (in our case, based on interpolated measurements), the forcing provided by the surface and aircraft data used here is dominated by $N_2O$ emissions. As a result, a model bias of up to 50 % in the stratospheric loss frequencies for $N_2O$ will have minimal impact on the inferred emissions given the inversion framework employed here.

Thompson et al. (2011) also examined the feasibility of constraining stratospheric loss rates of $N_2O$ using aircraft observations, but assumed zero model transport error in the observational error covariance matrix. We find that proper treatment of this error has a dramatic effect on the ability of the inversion framework to simultaneously retrieve emissions and stratospheric loss rates of $N_2O$. In the tests above, the model transport error was estimated based on the variance in $N_2O$ mixing ratios in the grid boxes adjacent to an observation; for aircraft observations near the tropopause, this variability can be an order of magnitude larger than it is near the surface. We find that when we omit the model transport error, the inversion is able to reduce an imposed prior bias in both emissions and stratospheric loss simultaneously, even when those biases have opposing effects on the $N_2O$ burden. As observed above, the same is not true when transport error is accounted for. Our ability to quantify both the emissions and chemistry of $N_2O$ based on aircraft data therefore depends critically on the accuracy of vertical transport in the model, and on the associated transport error assigned in the inversion.

Along with the rate of $N_2O$ destruction in the stratosphere, another factor that can affect $N_2O$ source inversions is model uncertainty in the mass flux of air between the stratosphere and troposphere (e.g., Thompson et al., 2014b). Our model framework,





GMDD
8, 5367–5418, 2015



employing assimilated meteorology, is not equipped to include this process directly as part of the state vector for optimization. However, we can explore the relative influence of chemistry vs. stratosphere–troposphere mixing on the tropospheric $N_2O$ burden (and hence on $N_2O$ source inversions) with the aid of a simple two-box model representing stratospheric and tropospheric reservoirs of $N_2O$. Such an analysis does not capture seasonal effects or spatial gradients within the troposphere and stratosphere, but nonetheless does illustrate some key features of the system.

Figure 7 shows the fractional perturbations to the stratospheric and tropospheric burdens of $N_2O$ in the box model that result from: (i) a 20 % increase in the global $N_2O$ emission source ($E$), (ii) a 20 % decrease in the photochemical loss rate of $N_2O$ ($k_{chem}$), and (iii) a 20 % decrease in the stratosphere–troposphere exchange rates ($k_{ST}$ and $k_{TS}$). For the latter, mass fluxes in both directions are increased proportionately since the (annual, global) $k_{ST}/k_{TS}$ ratio is known from the relative sizes of the troposphere and stratosphere.

The top panel of Fig. 7 shows that on long timescales a perturbation to $k_{ST}$ and $k_{TS}$ has a negligible effect on the tropospheric $N_2O$ burden compared to a perturbation to $k_{chem}$ or $E$. A given change in $k_{chem}$ or $E$ leads to a similar relative change in the steady-state burden, with an adjustment timescale dictated by the $N_2O$ lifetime (~ 127 years). In comparison, the effect of a change to $k_{TS}$ and $k_{ST}$ is small in the troposphere. For stratospheric $N_2O$, the effect of $k_{TS}$ and $k_{ST}$ is somewhat larger and of opposite sign: decreasing $k_{TS}$ and $k_{ST}$ reduces stratospheric $N_2O$ while increasing tropospheric $N_2O$.

However, on short timescales (as is used for our inversions), the importance of stratosphere–troposphere exchange vs. chemistry for tropospheric $N_2O$ is reversed, as the former manifests more quickly. The bottom panel of Fig. 7 indicates that for the first 2 years following a perturbation, the effect of $k_{TS}$ and $k_{ST}$ on the tropospheric $N_2O$ burden is 1.3–29× larger (mean: 5.1×) than the effect of $k_{chem}$. Over this same time period, Fig. 7 also shows that the effect of a perturbation to $k_{TS}$ and $k_{ST}$ is significant (mean: 0.8×) relative to a change in $E$. However, the importance of $k_{TS}$ and $k_{ST}$ vs. $E$





GMDD
8, 5367–5418, 2015



will be overstated by the box model as it does not resolve spatial gradients within the troposphere or the location of observations relative to emissions.

Overall, we can see that $N_2O$ source inversions based on the framework employed here will be unaffected by even relatively large model biases in the chemical loss rate of $N_2O$. The same does not apply to model biases in STE, and these need to be accounted for when evaluating a posteriori source estimates for $N_2O$ (Thompson et al., 2014b) and other long-lived species such as $CO_2$ (Deng et al., 2015).

### 5.3 Temporal resolution of $N_2O$ source inversions

The OSSEs in Sects. 5.1 and 5.2 demonstrate that the inversion (and $N_2O$ observing network) has a strong ability to remove model emission biases that are uniform in space and time. However, actual model emission errors are likely to be spatially and temporally dependent. For example, while the a priori natural soil and anthropogenic emissions used here are aseasonal, observations over an agricultural field in Ontario, Canada indicate that 30–90 % of the annual flux occurs in the non-growing season, mostly as strong pulses driven by soil thawing (Wagner-Riddle et al., 2007). Likewise, analysis of tall tower observations suggest a strong seasonal cycle of soil $N_2O$ emissions associated with the timing of fertilizer application (Miller et al., 2012; Griffis et al., 2013). A key question, therefore, is the following: at what spatial and temporal resolution can global $N_2O$ emissions be quantified based on the current observing network?

To explore the temporal aspect of this question, we performed a test in which we assimilate pseudo observations generated with aseasonal (model truth) emissions while imposing a simple seasonal bias in the a priori emissions from natural and agricultural soils (50 % higher than model truth from March–August; 50 % lower from September–February). As before, we assimilate surface, CARIBIC, or HIPPO observations, and retrieve monthly scaling factors for terrestrial and oceanic $N_2O$ emissions.

Results of this test indicate that a seasonal, global, emission bias is much more difficult to resolve than is a constant bias based on the current network of surface observations. Zonally-integrated emissions (Fig. S2) begin to approach the aseasonal





GMDD
8, 5367–5418, 2015



model truth in the Northern Hemisphere during the beginning of the simulation (when the prior emissions are biased high), but there is almost no correction of the seasonal bias in the latter half of the simulation (when prior emissions are biased low). Due to the long lifetime of $N_2O$, any residual high emission bias from the first portion of the simulation leads to positive model-measurement residuals even after the emission bias changes sign. Globally, the result is an annual flux that is biased slightly low (~ 5 %; Table 3) and with incorrect seasonality.

In areas near measurement sites, however, some seasonal constraints are afforded in the inversion. For example, Fig. 8 shows monthly fluxes at four locations: a site with continuous observations (KCMP Tall Tower), a site with flask observations (Hegyhátsál, Hungary), a location in eastern China that is upwind of surface flask observations, and a remote site in the Democratic Republic of Congo (DR Congo). At the beginning of the simulation there is a substantial correction of the emission bias at the in situ (KCMP), flask (Hungary), and upwind (East China) sites. During the latter half of the year, when the prior emissions are biased low, those errors are reduced as a result of the inversion at all three sites, but for the sites with measurements there is a time lag and subsequent overcorrection afterward. There is no significant correction to the biased DR Congo emissions during any point of the year.

Based on the above test, we can conclude that flask and in situ observations provide valuable corrections to seasonal emission biases upwind and in the vicinity of the measurements, though not necessarily on a monthly timescale. However, any seasonal biases arising from errors in model STE may be difficult to separate from such seasonal emission errors. Furthermore, large parts of the world (illustrated by the DR Congo site in Fig. 8) lack any meaningful seasonal constraints on emissions.

### 5.4 Spatial resolution of $N_2O$ source inversions

The spatial resolution at which current measurements constrain global $N_2O$ emissions in this inversion framework can be inferred from the reduction in emission errors that results from the inversion. Here, we calculate this relative error reduction from a stochas-





GMDD
8, 5367–5418, 2015



tic estimate of the inverse Hessian of the cost function (Eq. 1). For a reasonably linear model, the inverse Hessian approximates the posterior error covariance matrix of the emissions, and can be written:

$$(\nabla^2 J(\boldsymbol{x}))^{-1} = (\mathbf{S}_a^{-1} + \mathbf{H}^T \mathbf{S}_y^{-1} \mathbf{H})^{-1} \approx \mathbf{S}_{post} \quad (2)$$

where $\mathbf{H}$ is the tangent linear of the forward model, $\mathbf{S}_{post}$ is the posterior error covariance matrix, and $\mathbf{S}_a$ and $\mathbf{S}_y$ are the a priori and observational error covariance matrices, respectively, as in Eq. (1). Following Bousserez et al. (2015), we estimate $\nabla^2 J(\boldsymbol{x})$ using an ensemble (500 members here) of stochastic cost function gradients, each generated by adding Gaussian random noise to the pseudo observations according to the reported uncertainty of each dataset. The reduction in $\mathbf{S}_{post}(i,j)$ relative to $\mathbf{S}_a(i,j)$ for any model grid cell $(i,j)$ then represents the ability of our observing system to remove a random emission error in that location, in the absence of any large-scale source bias.

Figure 9 shows the resulting percent error reduction achieved in each model grid cell using surface, CARIBIC, or HIPPO observations for a given month of our two-year simulation. Results using surface observations are shown for month 1 (April 2010), but are comparable for all subsequent months. We see appreciable error reduction near sites with continuous observations in North America and Europe, and more modest error reductions in surrounding grid cells, at sites with flask observations, and in the northern Atlantic upwind of Europe. There is little ($< 5\,\%$) error reduction achieved throughout the tropics, Southern Hemisphere, and high latitudes, except near Cape Grim, Australia where continuous observations are available.

Figure 9 also shows that the sparse, high altitude CARIBIC observations provide limited information on the spatial distribution of $N_2O$ emissions. Significant error reduction is achieved over Western Europe during April 2010, the only month in which measurements were taken in the lower troposphere during special flights dedicated to volcano observation (Rauthe-Schöch, 2012). In all other months, measurements occur primar-





GMDD
8, 5367–5418, 2015



ily in the upper troposphere and lower stratosphere and consequently the spatial error reduction is minor (typically < 1 %).

The spatial information provided by HIPPO observations varies by month according to the flight tracks, and is complementary to that achieved with surface data. For example, during August 2011, we see large error reductions over the central US, as well as some improvement for grid cells in East Asia that are upwind of the HIPPO flight track. Some error reduction is also achieved in these locations for May 2011, despite the fact that no HIPPO flights occurred during this month (the next flights occurred in June). Given the long lifetime of $N_2O$, measurements in a given month thus provide some location-specific constraints on emissions in prior months. As is the case with the surface observations, however, the HIPPO data provides very little error reduction for emissions throughout the tropics, Southern Hemisphere and high latitudes. While the OSSE tests above showed that our observation and adjoint framework has significant skill in removing uniform model emission biases, we see in Fig. 9 that our current ability to allocate those $N_2O$ emissions spatially around the globe is in fact severely limited relative to the $4^\circ \times 5^\circ$ model resolution used here – and this is true for the airborne as well as the ground-based datasets.

Based on the same stochastic approach used above to calculate the inverse Hessian, we can also calculate the averaging kernel of the inversion to determine how well emissions in a given location can be independently resolved from emissions in other locations. If emissions in one location are completely resolved from those in other grid boxes, the averaging kernel value will be 1.0 in that location and 0 everywhere else. Here, we calculate the averaging kernel rows (based on the surface observations only) for a selected group of locations in key emission regions that vary in their proximity to $N_2O$ measurement sites.

Figure 10 shows the results for four locations: the KCMP Tall Tower (MN, USA; 44.68° N, 93.07° W), Hegyhátsál (Hungary; 46.95° N, 16.65° E), East China (30.0° N, 115.0° E), and the Democratic Republic of Congo (2.0° N, 30.0° E). KCMP features continuous observations, and we see that emissions in this model grid cell can be con-





GMDD
8, 5367–5418, 2015



strained independently (averaging kernel value near 1.0, and near 0.0 elsewhere) from those in other places. Significant constraints are achieved at Hegyhátsál (averaging kernel value $\sim 0.3$), where weekly flask observations are available, though some spatial smearing is apparent. Weaker constraints (averaging kernel values up to $\sim 0.03$) are achieved in the vicinity of the East China grid box, likely provided by downwind observations in Korea and the western Pacific.

Averaging kernel values for the Central Africa location are very low ($\sim 10^{-3}$), indicating little to no constraint on the source flux, and are also highly smeared spatially, showing that the current surface observations of $N_2O$ do not allow emissions in that region to be independently resolved from emissions elsewhere across the globe. We see in Fig. 10 that this spatial smearing even extends to the midlatitudes in both hemispheres. Emissions in the underconstrained tropics thus risk being conflated with those in other, distant source regions in global inversion analyses.

The implications of this current lack of constraints on tropical $N_2O$ emissions can be seen in a sample global inversion based on real atmospheric data. Figure 11 shows a posteriori emission scaling factors for global inversions based on two different assumptions: the first uses our previous construction of the a priori error covariance matrix (100 % uncertainty with horizontal correlation length scales of 500 km over land and 1000 km over ocean); the other does not include any penalty term (measuring the departure from a priori conditions) in the cost function. When a priori constraints are included, the solution is relatively spatially smooth. To correct for a low bias in our a priori emissions inventory, emissions increase throughout those terrestrial and oceanic regions where emissions occur, with a slightly higher inferred flux over South America. Conversely, when we eliminate the a priori constraint, emissions increase strongly in the tropics and Southern Hemisphere, reaching a factor of 10 (the upper bound placed on the scaling factors) in South America near the beginning of the two-year simulation. To compensate for this, the inferred emissions throughout the Northern Hemisphere decrease dramatically.





GMDD
8, 5367–5418, 2015



This severe sensitivity of the solution to the a priori error assumption reflects the ill-posed nature of the problem. It also highlights the fact that, because the global $N_2O$ flux is constrained (as the $N_2O$ lifetime and atmospheric burden are reasonably well-known), the lack of constraint on tropical emissions has important implications for understanding emissions elsewhere in the world.

### 5.5 Identifying priority locations for future $N_2O$ measurements

In this section, we apply the error reduction statistics derived above to identify priority regions where new observations are likely to have high value for improving present understanding of global $N_2O$ sources. To that end, we carry out forward model simulations in which $N_2O$ emissions in the first month are scaled by $(1 - \boldsymbol{x})$, where $\boldsymbol{x}$ is the spatial map of relative error reductions achieved in the inversion on the basis of the surface observations (e.g., Fig. 9). The initial atmospheric burden of $N_2O$ is set to zero, as are the emissions in subsequent months. The resulting atmospheric $N_2O$ then reflects unconstrained emissions, and the distribution of that "unconstrained $N_2O$" in space and time shows where new observations are needed to quantify those emissions in a spatially explicit way.

Figure 12 shows the distribution of unconstrained $N_2O$ mapped in the first and the second month following its emission. Results are shown for simulations starting in August 2010 and February 2011; these months were chosen to illustrate how seasonal differences in horizontal and vertical transport affect the atmospheric dispersion of underconstrained $N_2O$ emissions. In August, unconstrained mixing ratios above 1 ppb can be found throughout Southeast Asia, Central Africa, and South America, with the highest concentrations occurring over Brazil and off the western coasts of Africa and South America. Somewhat elevated concentrations (0.5–1 ppb) persist in these locations for the second month of the simulation, but these become well-dispersed in the following months (not shown). Unconstrained $N_2O$ emitted in August is initially concentrated in the lower troposphere in the tropics and northern midlatitudes, but is lofted through the tropical troposphere by September. In contrast, unconstrained $N_2O$ emitted in Febru-





GMDD
8, 5367–5418, 2015



ary is more strongly confined to the lower troposphere and the Northern Hemisphere, even a month after emission.

The maps in Fig. 12 rely by necessity on a particular prior estimate of $N_2O$ emissions and their distribution in space and time. However, they nonetheless provide an assessment of where additional measurements would have the best leverage for improving $N_2O$ emission estimates, based on our existing bottom-up understanding of when and where those emissions occur. We see in the maps that areas over or downwind of the tropics and East Asia should receive the highest measurement priority to reduce uncertainty in the overall $N_2O$ budget. As shown earlier, downwind surface observations can provide some spatially explicit emission constraints for regions with high fluxes; these may be the only feasible option for places where access, infrastructure, or political issues prevent sustained local measurements. We note that additional $N_2O$ measurements are available in and around Japan (Saikawa et al., 2013) that may provide additional constraints on East Asian emissions not achieved using the measurements presented here. In addition, aircraft measurements during the July–September timeframe should have strong value for constraining fluxes in the tropics, given the lofting and dispersal of those emissions that is apparent in the August 2010 simulation. On the other hand, Fig. 12 also reveals large areas of the world's oceans where additional surface measurements are not likely to provide appreciable new insights into the global $N_2O$ budget, given the lack of unconstrained $N_2O$ that is less than 1–2 months from emission.

## 6 Summary and conclusions

We developed a new inversion framework based on the GEOS-Chem model and its adjoint for estimating global $N_2O$ emissions and stratospheric loss rates using surface (flask; in-situ) as well as airborne (CARIBIC; HIPPO) measurements. We used this framework to: (i) quantify the ability of the current observing network to constrain the global distribution of $N_2O$ sources and sinks, (ii) assess the relative utility of the





GMDD
8, 5367–5418, 2015



various observing platforms for doing so, and (iii) identify priority locations where measurements are most needed to improve present understanding of the $N_2O$ budget. Our simulation period runs from April 2010 to April 2012, with initial conditions constructed using surface flask observations and vertical profile measurements from the MLS satellite sensor.

Observing system simulation experiments (OSSEs) showed that the surface and HIPPO observations can accurately resolve a uniform bias in $N_2O$ emissions for the first year of a two-year simulation; in comparison, the sparser (and mostly high altitude) CARIBIC observations provide a weaker constraint. All three datasets are able to independently resolve the global surface flux to within 5 % of the truth. On the other hand, a seasonal emission bias is much more difficult to resolve given the long lifetime of $N_2O$, particularly in regions with sparse observations. The surface observations do provide a reduction of seasonal emission errors in the vicinity of measurement sites and in large source regions upwind.

The surface and airborne datasets are all able to resolve a global bias in the stratospheric loss rate of $N_2O$ given known emissions, but do not give information on the spatial and temporal distribution of that sink. For the more realistic scenario with uncertain $N_2O$ sources and sink, we find that resolving the two in a joint source-sink inversion would require greater confidence in modeled transport than is currently warranted. Nevertheless, because of the timescale for stratosphere–troposphere mixing, $N_2O$ source inversions are insensitive to uncertainties in the chemical sink of $N_2O$ on the 2 year analysis time frame used here (and assuming an accurate initial state; e.g. from interpolated data). However, a simple box model analysis shows that tropospheric $N_2O$ is more sensitive to uncertainties in the rate of stratosphere–troposphere exchange (STE) than to those in the chemical loss rates for analysis timescales up to $\sim$ 3–4 years. Incomplete knowledge of STE rates will thus be a key source of uncertainty to address for $N_2O$ source inversions on these timescales.

We employed a stochastic estimate of the inverse Hessian to quantify the spatial resolution of $N_2O$ emission constraints afforded by the current global network of ob-





GMDD
8, 5367–5418, 2015



servations, and the degree to which emissions in a particular location can be distinguished from those elsewhere. Significant location-specific constraints are achieved in grid boxes near and immediately upwind of surface observation locations; however, these are mainly confined to North America, Europe and Australia. For sites with continuous surface observations, local emissions can be unambiguously resolved from those in surrounding locations, as indicated by large error reductions and averaging kernel (AK) values close to 1.0. Flask observations also provide significant local-to-regional constraints (e.g., AK values of $\sim 0.3$ at a site with weekly measurements). HIPPO observations primarily provide emission constraints for the Central US and East Asia. Critically, little to no spatial information on tropical emissions is provided by either set of observations: the corresponding AKs are highly smeared spatially and show that emissions in many parts of the tropics cannot even be resolved from those in the mid-latitudes. For global inversions, this underconstraint in the tropics can thus lead to large errors in the inferred $N_2O$ fluxes for the extratropics as well as the tropics themselves.

From the atmospheric distribution of "unconstrained $N_2O$" simulated based on the error reduction statistics achieved in the inversion and our a priori source estimates, we identify areas in the tropics and East Asia as the highest priorities for new $N_2O$ measurements to advance understanding of the global budget. In situ or flask observations downwind of major sources in South America, Central Africa, and East Asia can provide some spatial information on $N_2O$ fluxes in cases where local, long-term measurements are impractical. Targeted aircraft measurements in the troposphere could also provide much-needed constraints on tropical emission fluxes, particularly during July–September when emissions are well-lofted vertically.

From our analysis it is clear that additional measurements are crucial to obtaining a more complete picture of global $N_2O$ sources, particularly in the key areas mentioned above. In this context, we will further investigate the use of efficient randomization techniques to estimate the spatiotemporal constraints provided by new and existing $N_2O$ measurements, and design optimal dimension approaches for $N_2O$ source inversions. Such work could also include an evaluation of information provided by new $N_2O$





GMDD
8, 5367–5418, 2015



retrievals from AIRS (Xiong et al., 2014) and other space-based infrared sounders. The fact that the current observing system yields little information on the space–time distribution of $N_2O$ fluxes over large parts of the world also speaks to the need for process-based emission models that can provide a priori source estimates that faithfully capture the key modes of variability. Such models are also needed to project how soil $N_2O$ fluxes will respond to future changes in climate, hydrology, and nitrogen deposition and runoff.

## Code availability

The $N_2O$ version of the GEOS-Chem adjoint code is available via the GEOS-Chem adjoint repository. Instructions for obtaining access to the code can be found at wiki.seas.harvard.edu/geos-chem/index.php/GEOS-Chem_Adjoint.

**The Supplement related to this article is available online at doi:10.5194/gmdd-8-5367-2015-supplement.**

*Acknowledgements.* This work was supported by NOAA (grant no. NA13OAR4310086) and the Minnesota Supercomputing Institute. We thank J. Muhle and C. Harth (UCSD-SIO), D. Young (U. Bristol), P. Fraser (CSIRO), R. Wang (GaTech), and other members of the AGAGE team for providing AGAGE data. The 6 AGAGE stations used here are supported principally by NASA (USA) grants to MIT and SIO, and also by DECC (UK) and NOAA (USA) grants to Bristol University, and by CSIRO and BoM (Australia). We thank Environment Canada for providing data from the Churchill, Estevan Point, East Trout Lake, Fraserdale, and Sable Island sites. We thank R. Martin and S. Nichol for providing data from the Arrival Heights NIWA station.





GMDD
8, 5367–5418, 2015



## References


Assonov, S. S., Brenninkmeijer, C. A. M., Schuck, T., and Umezawa, T.: $N_2O$ as a tracer of mixing stratospheric and tropospheric air based on CARIBIC data with applications for $CO_2$, Atmos. Environ., 79, 769–779, doi:10.1016/j.atmosenv.2013.07.035, 2013.

Bousserez, N., Henze, D. K., Perkins, A., Bowman, K. W., Lee, M., Liu, J., Deng, F., and Jones, D. B. A.: Improved analysis-error covariance matrix for high-dimensional variational inversions: application to source estimation using a 3D atmospheric transport model, Q. J. Roy. Meteor. Soc., doi:10.1002/qj.2495, online first, 2015.

Bouwman, A. F.: Environmental science – nitrogen oxides and tropical agriculture, Nature, 392, 866–867, doi:10.1038/31809, 1998.

Bouwman, A. F., Beusen, A. H. W., Griffioen, J., Van Groenigen, J. W., Hefting, M. M., Oenema, O., Van Puijenbroek, P. J. T. M., Seitzinger, S., Slomp, C. P., and Stehfest, E.: Global trends and uncertainties in terrestrial denitrification and $N_2O$ emissions, Philos. T. Roy Soc. B, 368, 20130112, doi:10.1098/rstb.2013.0112, 2013.

Brenninkmeijer, C. A. M., Crutzen, P., Boumard, F., Dauer, T., Dix, B., Ebinghaus, R., Filippi, D., Fischer, H., Franke, H., Frieß, U., Heintzenberg, J., Helleis, F., Hermann, M., Kock, H. H., Koeppel, C., Lelieveld, J., Leuenberger, M., Martinsson, B. G., Miemczyk, S., Moret, H. P., Nguyen, H. N., Nyfeler, P., Oram, D., O'Sullivan, D., Penkett, S., Platt, U., Pupek, M., Ramonet, M., Randa, B., Reichelt, M., Rhee, T. S., Rohwer, J., Rosenfeld, K., Scharffe, D., Schlager, H., Schumann, U., Slemr, F., Sprung, D., Stock, P., Thaler, R., Valentino, F., van Velthoven, P., Waibel, A., Wandel, A., Waschitschek, K., Wiedensohler, A., Xueref-Remy, I., Zahn, A., Zech, U., and Ziereis, H.: Civil Aircraft for the regular investigation of the atmosphere based on an instrumented container: The new CARIBIC system, Atmos. Chem. Phys., 7, 4953–4976, doi:10.5194/acp-7-4953-2007, 2007.

Butterbach-Bahl, K., Baggs, E. M., Dannenmann, M., Kiese, R., and Zechmeister-Boltenstern, S.: Nitrous oxide emissions from soils: how well do we understand the processes and their controls?, Philos. T. Roy Soc. B, 368, 20140122, doi:10.1098/rstb.2013.0122, 2013.

Byrd, R. H., Lu, P. H., Nocedal, J., and Zhu, C. Y.: A limited memory algorithm for bound constrained optimization, SIAM J. Sci. Comput., 16, 1190–1208, doi:10.1137/0916069, 1995.

Cohen, Y. and Gordon, L. I.: Nitrous oxide production in the ocean, J. Geophys. Res.-Oc. Atm., 84, 347–353, doi:10.1029/JC084iC01p00347, 1979.






GMDD
8, 5367–5418, 2015



Cooper, L. N., Steele, L. P., Langenfelds, R. L., Spencer, D. A., and Lucarelli, M. P.: Atmospheric methane, carbon dioxide, hydrogen, carbon monoxide and nitrous oxide from Cape Grim flask air samples analysed by gas chromatography, Baseline Atmospheric Program (Australia) 1996, 98–102, Bureau of Meteorology and CSIRO Atmosphric Research, 1999.

Davidson, E. A.: The contribution of manure and fertilizer nitrogen to atmospheric nitrous oxide since 1860, Nat. Geosci., 2, 659–662, doi:10.1038/ngeo608, 2009.

Deng, F., Jones, D. B. A., Walker, T. W., Keller, M., Bowman, K. W., Henze, D. K., Nassar, R., Kort, E. A., Wofsy, S. C., Walker, K. A., Bourassa, A. E., and Degenstein, D. A.: Sensitivity analysis of the potential impact of discrepancies in stratosphere–troposphere exchange on inferred sources and sinks of $CO_2$, Atmos. Chem. Phys. Discuss., 15, 10813–10851, doi:10.5194/acpd-15-10813-2015, 2015.

Denman, K. L., Brasseur, G. P., Chidthaisong, A., Ciais, P., Cox, P. M., Dickinson, R. E., Hauglustaine, D., Heinze, C., Holland, E., Jacob, D., Lohmann, U., Ramachandran, S., da Silva Dias, P. L., Wofsy, S. C., and Zhang, X.: Couplings between changes in the climate system and biogeochemistry, in: Climate Change 2007: Contribution of Working Group I to the Fourth Assessment Report of the Intergovernmental Panel on Climate Change, edited by: Solomon, S. D., Qin, D., Manning, M., Chen, Z., Marquis, M., Averyt, K. B., Tignor, M., and Miller, H. L., Cambridge University Press, Cambridge, 499–587, 2007.

Dlugokencky, E. J., Steele, L. P., Lang, P. M., and Masarie, K. A.: The growth rate and distrubution of atmospheric methane, J. Geophys. Res.-Atmos., 99, 17021–17043, doi:10.1029/94JD01245, 1994.

Firestone, M. K. and Davidson, E. A.: Microbiological basis of NO and $N_2O$ production and consumption in the soil, in: Exchange of Trace Gases Between Terrestrial Ecosystems and the Atmosphere, edited by: Andreae, M. O. and Schimel, D. S., Wiley and Sons, Chichester, 7–21, 1989.

Forster, P., Ramaswamy, V., Artaxo, P., Berntsen, T., Betts, R., Fahey, D. W., Haywood, J., Lean, J., Lowe, D. C., Myrhe, G., Nganga, J., Prinn, R., Raga, G., Schulz, M., and Van Dorland, R.: Changes in atmospheric constituents and in radiative forcing, in: Climate Change 2007: the Physical Science Basis. Contribution of Working Group I to the Fourth Assessment Report of the Intergovernmental Panel on Climate Change, Cambridge University Press, Cambridge, UK, New York, NY, USA, 2007.

Elkins, J. W., Wofsy, S. C., McElroy, M. B., Kolb, C. E., and Kaplan, W. A.: Aquatic sources and sinks for nitrous oxide, Nature, 275, 602–606, 1978.





GMDD
8, 5367–5418, 2015



Francey, R. J., Steele, L. P., Langenfelds, R. L., Lucarelli, M. P., Allison, C. E., Beardsmore, D. J., Coram, S. A., Derek, N., de Silva, F. R., Etheridge, D. M., Fraser, P. J., Henry, R. J., Turner, B., Welch, E. D., Spencer, D. A., and Cooper, L. N.,: Global Atmospheric Sampling Laboratory (GASLAB): supporting and extending the Cape Grim trace gas programs, Baseline Atmospheric Program (Australia) 1993, 8–29, Bureau of Meteorology and CSIRO division of Atmospheric Research, 1996.

Galloway, J. N., Townsend, A. R., Erisman, J. W., Bekunda, M., Cai, Z. C., Freney, J. R., Martinelli, L. A., Seitzinger, S. P., and Sutton, M. A.: Transformation of the nitrogen cycle: recent trends, questions, and potential solutions, Science, 320, 889–892, doi:10.1126/science.1136674, 2008.

Griffis, T. J., Lee, X., Baker, J. M., Russelle, M. P., Zhang, X., Venterea, R., and Millet, D. B.: Reconciling the differences between top-down and bottom-up estimates of nitrous oxide emissions for the US Corn Belt, Global Biogeochem. Cy., 27, 746–754, doi:10.1002/gbc.20066, 2013.

Henze, D. K., Hakami, A., and Seinfeld, J. H.: Development of the adjoint of GEOS-Chem, Atmos. Chem. Phys., 7, 2413–2433, doi:10.5194/acp-7-2413-2007, 2007.

Henze, D. K., Seinfeld, J. H., and Shindell, D. T.: Inverse modeling and mapping US air quality influences of inorganic $PM_{2.5}$ precursor emissions using the adjoint of GEOS-Chem, Atmos. Chem. Phys., 9, 5877–5903, doi:10.5194/acp-9-5877-2009, 2009.

Hirsch, A. I., Michalak, A. M., Bruhwiler, L. M., Peters, W., Dlugokencky, E. J., and Tans, P. P.: Inverse modeling estimates of the global nitrous oxide surface flux from 1998–2001, Global Biogeochem. Cy., 20, GB1008, doi:10.1029/2004gb002443, 2006.

Huang, J., Golombek, A., Prinn, R., Weiss, R., Fraser, P., Simmonds, P., Dlugokencky, E. J., Hall, B., Elkins, J., Steele, P., Langenfelds, R., Krummel, P., Dutton, G., and Porter, L.: Estimation of regional emissions of nitrous oxide from 1997 to 2005 using multinetwork measurements, a chemical transport model, and an inverse method, J. Geophys. Res., 113, D17313, doi:10.1029/2007JD009381, 2008.

IPCC: 2006 IPCC Guidelines for National Greenhouse Gas Inventories, edited by: Eggleston, H. S., Buendia, L., Miwa, K., Ngara, T., and Tanabe, K., IGES, Japan, 2006.

Jiang, Z., Jones, D. B. A., Kopacz, M., Liu, J., Henze, D. K., and Heald, C.: Quantifying the impact of model errors on top-down estimates of carbon monoxide emissions using satellite observations, J. Geophys. Res.-Atmos, 116, D15306, doi:10.1029/2010JD015282, 2011.





GMDD
8, 5367–5418, 2015



Jiang, Z., Jones, D. B. A., Worden, H. M., Deeter, M. N., Henze, D. K., Worden, J., Bowman, K. W., Brenninkmeijer, C. A. M., and Schuck, T. J.: Impact of model errors in convective transport on CO source estimates inferred from MOPITT CO retrievals, J. Geophys. Res., 118, 2073–2083, doi:10.1002/jgrd.50216, 2013.

Jin, X. and Gruber, N.: Offsetting the radiative benefit of ocean iron fertilization by enhancing $N_2O$ emissions, Geophys. Res. Lett., 30, 2249, doi:10.1029/2003GL018458, 2003.

Kopacz, M., Jacob, D. J., Henze, D. K., Heald, C. L., Streets, D. G., and Zhang, Q.: Comparison of adjoint and analytical Bayesian inversion methods for constraining Asian sources of carbon monoxide using satellite (MOPITT) measurements of CO columns, J. Geophys. Res.-Atmos., 114, D04305, doi:10.1029/2007JD009264, 2009.

Kopacz, M., Jacob, D. J., Fisher, J. A., Logan, J. A., Zhang, L., Megretskaia, I. A., Yantosca, R. M., Singh, K., Henze, D. K., Burrows, J. P., Buchwitz, M., Khlystova, I., McMillan, W. W., Gille, J. C., Edwards, D. P., Eldering, A., Thouret, V., and Nedelec, P.: Global estimates of CO sources with high resolution by adjoint inversion of multiple satellite datasets (MOPITT, AIRS, SCIAMACHY, TES), Atmos. Chem. Phys., 10, 855–876, doi:10.5194/acp-10-855-2010, 2010.

Kopacz, M., Mauzerall, D. L., Wang, J., Leibensperger, E. M., Henze, D. K., and Singh, K.: Origin and radiative forcing of black carbon transported to the Himalayas and Tibetan Plateau, Atmos. Chem. Phys., 11, 2837–2852, doi:10.5194/acp-11-2837-2011, 2011.

Kort, E. A., Patra, P. K., Ishijima, K., Daube, B. C., Jimenez, R., Elkins, J., Hurst, D., Moore, F. L., Sweeney, C., and Wofsy, S. C.: Tropospheric distribution and variability of $N_2O$: evidence for strong tropical emissions, Geophys. Res. Lett., 38, L15806, doi:10.1029/2011GL047612, 2011.

Lambert, A., Read, W. G., Livesey, N. J., Santee, M. L., Manney, G. L., Froidevaux, L., Wu, D. L., Schwartz, M. J., Pumphrey, H. C., Jimenez, C., Nedoluha, G. E., Cofield, R. E., Cuddy, D. T., Daffer, W. H., Drouin, B. J., Fuller, R. A., Jarnot, R. F., Knosp, B. W., Pickett, H. M., Perun, V. S., Snyder, W. V., Stek, P. C., Thurstans, R. P., Wagner, P. A., Waters, J. W., Jucks, K. W., Toon, G. C., Stachnik, R. A., Bernath, P. F., Boone, C. D., Walker, K. A., Urban, J., Murtagh, D., Elkins, J. W., and Atlas, E.: Validation of the Aura Microwave Limb Sounder middle atmosphere water vapor and nitrous oxide measurements, J. Geophys. Res.-Atmos., 112, D24S36, doi:10.1029/2007JD008724, 2007.

Law, C. S. and Owens, N. J. P.: Significant flux of atmospheric nitrous oxide from the northwest Indian Ocean, Nature, 346, 826–828, doi:10.1038/346826a0, 1990.





GMDD
8, 5367–5418, 2015



Maggiotto, S. R., Webb, J. A., Wagner-Riddle, C., and Thurtell, G. W.: Nitrous and nitrogen oxide emissions from turfgrass receiving different forms of nitrogen fertilizer, J. Environ. Qual., 29, 621–630, 2000.

Miller, S. M., Kort, E. A., Hirsch, A. I., Dlugokencky, E. J., Andrews, A. E., Xu, X., Tian, H., Nehrkorn, T., Eluszkiewicz, J., Michalak, A. M., and Wofsy, S. C.: Regional sources of nitrous oxide over the United States: seasonal variation and spatial distribution, J. Geophys. Res.-Atmos., 117, D06310, doi:10.1029/2011JD016951, 2012.

Mosier, A., Kroeze, C., Nevison, C., Oenema, O., Seitzinger, S., and van Cleemput, O.: Closing the global $N_2O$ budget: nitrous oxide emissions through the agricultural nitrogen cycle – OECD/IPCC/IEA phase II development of IPCC guidelines for national greenhouse gas inventory methodology, Nutr. Cycl. Agroecosys., 52, 225–248, doi:10.1023/a:1009740530221, 1998.

Nevison, C. D., Keeling, R. F., Weiss, R. F., Popp, B. N., Jin, X., Fraser, P. J., Porter, L. W., and Hess, P. G.: Southern Ocean ventilation inferred from seasonal cycles of atmospheric $N_2O$ and $O_2/N_2$ at Cape Grim, Tasmania, Tellus B, 57, 218–229, doi:10.1111/j.1600-0889.2005.00143.x, 2005.

Nevison, C. D., Dlugokencky, E., Dutton, G., Elkins, J. W., Fraser, P., Hall, B., Krummel, P. B., Langenfelds, R. L., O'Doherty, S., Prinn, R. G., Steele, L. P., and Weiss, R. F.: Exploring causes of interannual variability in the seasonal cycles of tropospheric nitrous oxide, Atmos. Chem. Phys., 11, 3713–3730, doi:10.5194/acp-11-3713-2011, 2011.

Park, S., Croteau, P., Boering, K. A., Etheridge, D. M., Ferretti, D., Fraser, P. J., Kim, K. R., Krummel, P. B., Langenfelds, R. L., van Ommen, T. D., Steele, L. P., and Trudinger, C. M.: Trends and seasonal cycles in the isotopic composition of nitrous oxide since 1940, Nat. Geosci., 5, 261–265, doi:10.1038/ngeo1421, 2012.

Parrington, M., Palmer, P. I., Henze, D. K., Tarasick, D. W., Hyer, E. J., Owen, R. C., Helmig, D., Clerbaux, C., Bowman, K. W., Deeter, M. N., Barratt, E. M., Coheur, P.-F., Hurtmans, D., Jiang, Z., George, M., and Worden, J. R.: The influence of boreal biomass burning emissions on the distribution of tropospheric ozone over North America and the North Atlantic during 2010, Atmos. Chem. Phys., 12, 2077–2098, doi:10.5194/acp-12-2077-2012, 2012.

Potter, C. S., Matson, P. A., Vitousek, P. M., and Davidson, E. A.: Process modeling of controls on nitrogen trace gas emissions from soils worldwide, J. Geophys. Res.-Atmos., 101, 1361–1377, doi:10.1029/95JD02028, 1996.





GMDD
8, 5367–5418, 2015



Prather, M. J., Holmes, C. D., and Hsu, J.: Reactive greenhouse gas scenarios: systematic exploration of uncertainties and the role of atmospheric chemistry, Geophys. Res. Lett., 39, L09803, doi:10.1029/2012GL051440, 2012.

Prinn, R. G., Weiss, R. F., Fraser, P. J., Simmonds, P. G., Cunnold, D. M., Alyea, F. N., O'Doherty, S., Salameh, P., Miller, B. R., Huang, J., Wang, R. H. J., Hartley, D. E., Harth, C., Steele, L. P., Sturrock, G., Midgley, P. M., and McCulloch, A.: A history of chemically and radiatively important gases in air deduced from ALE/GAGE/AGAGE, J. Geophys. Res., 105, 17751–17792, doi:10.1029/2000JD900141, 2000.

Rauthe-Schöch, A., Weigelt, A., Hermann, M., Martinsson, B. G., Baker, A. K., Heue, K.-P., Brenninkmeijer, C. A. M., Zahn, A., Scharffe, D., Eckhardt, S., Stohl, A., and van Velthoven, P. F. J.: CARIBIC aircraft measurements of Eyjafjallajökull volcanic clouds in April/May 2010, Atmos. Chem. Phys., 12, 879–902, doi:10.5194/acp-12-879-2012, 2012.

Ravishankara, A. R., Daniel, J. S., and Portmann, R. W.: Nitrous oxide ($N_2O$): the dominant ozone-depleting substance emitted in the 21st century, Science, 326, 123–125, doi:10.1126/science.1176985, 2009.

Saikawa, E., Prinn, R. G., Dlugokencky, E., Ishijima, K., Dutton, G. S., Hall, B. D., Langenfelds, R., Tohjima, Y., Machida, T., Manizza, M., Rigby, M., O'Doherty, S., Patra, P. K., Harth, C. M., Weiss, R. F., Krummel, P. B., van der Schoot, M., Fraser, P. J., Steele, L. P., Aoki, S., Nakazawa, T., and Elkins, J. W.: Global and regional emissions estimates for $N_2O$, Atmos. Chem. Phys., 14, 4617–4641, doi:10.5194/acp-14-4617-2014, 2014.

Salstein, D. A.: Mean properties of the atmosphere, in: Composition, Chemistry, and Climate of the Atmosphere, edited by: Singh, H. B., Van Nostrand Reinhold, New York, 19–49, 1995.

Schuck, T. J., Brenninkmeijer, C. A. M., Slemr, F., Xueref-Remy, I., and Zahn, A.: Greenhouse gas analysis of air samples collected onboard the CARIBIC passenger aircraft, Atmos. Meas. Tech., 2, 449–464, doi:10.5194/amt-2-449-2009, 2009.

Shcherbak, I., Millar, N., and Robertson, G. P.: Global metaanalysis of the nonlinear response of soil nitrous oxide ($N_2O$) emissions to fertilizer nitrogen, P. Natl. Acad. Sci. USA, 111, 9199–9204, doi:10.1073/pnas.1322434111, 2014.

Thompson, R. L., Bousquet, P., Chevallier, F., Rayner, P. J., and Ciais, P.: Impact of the atmospheric sink and vertical mixing on nitrous oxide fluxes estimated using inversion methods, J. Geophys. Res.-Atmos., 116, D17307, doi:10.1029/2011JD015815, 2011.

Thompson, R. L., Chevallier, F., Crotwell, A. M., Dutton, G., Langenfelds, R. L., Prinn, R. G., Weiss, R. F., Tohjima, Y., Nakazawa, T., Krummel, P. B., Steele, L. P., Fraser, P., O'Doherty, S.,





GMDD
8, 5367–5418, 2015



Ishijima, K., and Aoki, S.: Nitrous oxide emissions 1999 to 2009 from a global atmospheric inversion, Atmos. Chem. Phys., 14, 1801–1817, doi:10.5194/acp-14-1801-2014, 2014a.

Thompson, R. L., Patra, P. K., Ishijima, K., Saikawa, E., Corazza, M., Karstens, U., Wilson, C., Bergamaschi, P., Dlugokencky, E., Sweeney, C., Prinn, R. G., Weiss, R. F., O'Doherty, S., Fraser, P. J., Steele, L. P., Krummel, P. B., Saunois, M., Chipperfield, M., and Bousquet, P.: TransCom $N_2O$ model inter-comparison – Part 1: Assessing the influence of transport and surface fluxes on tropospheric $N_2O$ variability, Atmos. Chem. Phys., 14, 4349–4368, doi:10.5194/acp-14-4349-2014, 2014b.

Thompson, R. L., Ishijima, K., Saikawa, E., Corazza, M., Karstens, U., Patra, P. K., Bergamaschi, P., Chevallier, F., Dlugokencky, E., Prinn, R. G., Weiss, R. F., O'Doherty, S., Fraser, P. J., Steele, L. P., Krummel, P. B., Vermeulen, A., Tohjima, Y., Jordan, A., Haszpra, L., Steinbacher, M., Van der Laan, S., Aalto, T., Meinhardt, F., Popa, M. E., Moncrieff, J., and Bousquet, P.: TransCom $N_2O$ model inter-comparison – Part 2: Atmospheric inversion estimates of $N_2O$ emissions, Atmos. Chem. Phys., 14, 6177–6194, doi:10.5194/acp-14-6177-2014, 2014.

Umezawa, T., Baker, A. K., Oram, D., Sauvage, C., O'Sullivan, D., Rauthe-Schoch, A., Montzka, S. A., Zahn, A., and Brenninkmeijer, C. A. M.: Methyl chloride in the upper troposphere observed by CARIBIC passenger aircraft observatory: large-scale distributions and Asian summer monsoon outflow, J. Geophys. Res.-Atmos., 119, 5542–5558, doi:10.1002/2013JD021396, 2014.

van der Werf, G. R., Randerson, J. T., Giglio, L., Collatz, G. J., Mu, M., Kasibhatla, P. S., Morton, D. C., DeFries, R. S., Jin, Y., and van Leeuwen, T. T.: Global fire emissions and the contribution of deforestation, savanna, forest, agricultural, and peat fires (1997–2009), Atmos. Chem. Phys., 10, 11707–11735, doi:10.5194/acp-10-11707-2010, 2010.

Volk, C. M., Elkins, J. W., Fahey, D. W., Dutton, G. S., Gilligan, J. M., Loewenstein, M., Podolske, J. R., Chan, K. R., and Gunson, M. R.: Evaluation of source gas lifetimes from stratospheric observations, J. Geophys. Res.-Atmos., 102, 25543–25564, doi:10.1029/97JD02215, 1997.

Wagner-Riddle, C., Furon, A., McLaughlin, N. L., Lee, I., Barbeau, J., Jayasundara, S., Parkin, G., Von Bertoldi, P., and Warland, J.: Intensive measurement of nitrous oxide emissions from a corn-soybean-wheat rotation under two contrasting management systems over 5 years, Glob. Change Biol., 13, 1722–1736, doi:10.1111/j.1365-2486.2007.01388.x, 2007.





GMDD
8, 5367–5418, 2015



Wang, J., Xu, X., Henze, D. K., Zeng, J., Ji, Q., Tsay, S.-C., and Huang, J.: Top-down estimate of dust emissions through integration of MODIS and MISR aerosol retrievals with the GEOS-Chem adjoint model, Geophys. Res. Lett., 39, L08802, doi:10.1029/2012GL051136, 2012.
Wells, K. C., Millet, D. B., Cady-Pereira, K. E., Shephard, M. W., Henze, D. K., Bousserez, N., Apel, E. C., de Gouw, J., Warneke, C., and Singh, H. B.: Quantifying global terrestrial methanol emissions using observations from the TES satellite sensor, Atmos. Chem. Phys., 14, 2555–2570, doi:10.5194/acp-14-2555-2014, 2014.
Wofsy, S. C.: HIAPER Pole-to-Pole Observations (HIPPO): fine-grained, global-scale measurements of climatically important atmospheric gases and aerosols, Philos. T. Roy. Soc. A, 369, 2073–2086, doi:10.1098/rsta.2010.0313, 2011.
Xiong, X., Maddy, E. S., Barnet, C., Gambacorta, A., Patra, P. K., Sun, F., and Goldberg, M.: Retrieval of nitrous oxide from Atmospheric Infrared Sounder: characterization and validation, J. Geophys. Res.-Atmos., 119, 9107–9122, doi:10.1002/2013JD021406, 2014.
Xu, X., Wang, J., Henze, D. K., Qu, W., and Kopacz, M.: Constraints on aerosol sources using GEOS-Chem adjoint and MODIS radiances, and evaluation with multisensor (OMI, MISR) data, J. Geophys. Res.-Atmos., 118, 6396–6413, doi:10.1002/jgrd.50515, 2013.
Zhang, L., Jacob, D. J., Kopacz, M., Henze, D. K., Singh, K., and Jaffe, D. A.: Intercontinental source attribution of ozone pollution at western US sites using an adjoint method, Geophys. Res. Lett., 36, L11810, doi:10.1029/2009GL037950, 2009.
Zhu, C., Byrd, R. H., Lu, P., and Nocedal, J.: L-BFGS-B: a limited memory FORTRAN code for solving bound constrained optimization problems, Tech. rep., Northwestern University, 1994.
Zhu, L., Henze, D. K., Cady-Pereira, K. E., Shephard, M. W., Luo, M., Pinder, R. W., Bash, J. O., and Jeong, G. R.: Constraining U.S. ammonia emissions using TES remote sensing observations and the GEOS-Chem adjoint model, J. Geophys. Res.-Atmos, 118, 3355–3368, doi:10.1002/jgrd.50166, 2013.





GMDD
8, 5367–5418, 2015



**Table 1.** $N_2O$ emissions in the a priori database and their global annual totals.

| Sector | IPCC code | Global annual source ($Tg\,N\,yr^{-1}$) |
|---|---|---|
| Agricultural soil[a] | 4C + 4D | 3.97 |
| Indirect emissions from agriculture[a] | 4D3 | 0.57 |
| Energy manufacturing transformation[a] | 1A1 + 1A2 + 1B1b | 0.21 |
| Non-road transportation[a] | 1A3a + c + d + e | 5.0E-2 |
| Road transportation[a] | 1A3b | 0.14 |
| Oil production and refineries[a] | 1B2a | 4.2E-3 |
| Industrial process and product use[a] | 2 | 0.85 |
| Fossil fuel fires[a] | 7A | 4.8E-4 |
| Manure management[a] | 4B | 0.21 |
| Residential[a] | 1A4 | 0.18 |
| Waste solid and waste water[a] | 6 | 0.24 |
| Indirect $N_2O$ from $NO_x$ and $NH_3$[a] | 7B + 7C | 0.45 |
| **Total anthropogenic**[a] | | **6.9** |
| **Total natural soil**[b] | | **3.2** |
| **Total biomass burning**[c] | | **0.6** |
| **Total net ocean**[d] | | **3.5** |

[a] From EDGARv4.2 for 2008.
[b] From EDGARv2 for 1990.
[c] From GFEDv3 (van der Werf et al., 2010).
[d] From Jin and Gruber (2003).





GMDD
8, 5367–5418, 2015



**Table 2.** Sites of surface flask and in situ $N_2O$ observations used in this study.

| Location | Latitude | Longitude | Network* | Measurement type | Measurement scale |
|---|---|---|---|---|---|
| Arrival Heights, Antarctica | −77.80 | 166.67 | NIWA | Flask | NOAA 2006A |
| Alert, Nunavut, Canada | 82.45 | −62.51 | CCGG | Flask | NOAA 2006A |
| Argyle, Maine, USA | 45.04 | −68.68 | CCGG | Flask | NOAA 2006A |
| Ascension Island | −7.97 | −14.40 | CCGG | Flask | NOAA 2006A |
| Assekrem, Algeria | 23.26 | 5.63 | CCGG | Flask | NOAA 2006A |
| Tereceira Island, Azores | 38.77 | −27.38 | CCGG | Flask | NOAA 2006A |
| Baltic Sea, Poland | 55.35 | 17.22 | CCGG | Flask | NOAA 2006A |
| Boulder Atmospheric Observatory, Colorado, USA | 40.05 | −105.00 | CCGG | Flask | NOAA 2006A |
| Baring Head, New Zealand | −41.41 | 174.87 | CCGG | Flask | NOAA 2006A |
| Bukit Kototabang, Indonesia | −0.20 | 100.32 | CCGG | Flask | NOAA 2006A |
| St. David's Head, Bermuda | 32.37 | −64.65 | CCGG | Flask | NOAA 2006A |
| Tudor Hill, Bermuda | 32.27 | −64.88 | CCGG | Flask | NOAA 2006A |
| Barrow, Alaska, USA | 71.32 | −156.61 | CCGG, CATS | Flask, in situ | NOAA 2006A |
| Black Sea, Constanta, Romania | 44.18 | 28.67 | CCGG | Flask | NOAA 2006A |
| Cold Bay, Alaska, USA | 55.21 | −162.72 | CCGG | Flask | NOAA 2006A |
| Cape Ferguson, Australia | −19.28 | 147.05 | CSIRO | Flask | NOAA 2006A |
| Cape Grim, Tasmania, Australia | −40.68 | 144.69 | CCGG, AGAGE | Flask, in situ | NOAA 2006A, SIO-98 |
| Churchill, Manitoba, Canada | 58.75 | −94.07 | EC | Flask | NOAA 2006 |
| Christmas Island | 1.70 | −157.15 | CCGG | Flask | NOAA 2006A |
| Cape Rama, India | 15.08 | 73.83 | CSIRO | Flask | NOAA 2006A |
| Crozet Island | −46.43 | 51.85 | CCGG | Flask | NOAA 2006A |
| Casey Station, Antarctica | −66.28 | 110.53 | CSIRO | Flask | NOAA 2006A |
| Drake Passage | −59.00 | −64.69 | CCGG | Flask | NOAA 2006A |
| Easter Island | −27.16 | −109.43 | CCGG | Flask | NOAA 2006A |
| Estevan Point, British Columbia, Canada | 49.38 | −126.55 | EC | Flask | NOAA 2006 |
| East Trout Lake, Saskatchewan, Canada | 54.33 | −104.98 | EC | Flask | NOAA 2006 |
| Fraserdale, Ontario, Canada | 49.88 | −81.57 | EC | Flask | NOAA 2006 |
| Mariana Islands, Guam | 13.39 | 144.66 | CCGG | Flask | NOAA 2006A |
| Gunn Point, Australia | −12.25 | 131.05 | CSIRO | Flask | NOAA 2006A |
| Halley Station, Antarctica | −75.61 | −26.21 | CCGG | Flask | NOAA 2006A |
| Hohenpeissenberg, Germany | 47.80 | 11.02 | CCGG | Flask | NOAA 2006A |
| Hegyhátsál, Hungary | 46.95 | 16.65 | CCGG | Flask | NOAA 2006A |
| Stórhofdi, Vestmannaeyjar, Iceland | 63.40 | −20.29 | CCGG | Flask | NOAA 2006A |
| Izaña, Tenerife, Canary Islands | 28.31 | −16.50 | CCGG | Flask | NOAA 2006A |
| Jungfraujoch, Switzerland | 46.55 | 7.99 | AGAGE | In situ | SIO-98 |
| Key Biscayne, Florida, USA | 25.67 | −80.16 | CCGG | Flask | NOAA 2006A |
| Cape Kumukahi, Hawaii, USA | 19.52 | −154.82 | CCGG | Flask | NOAA 2006A |
| Park Falls, Wisconsin, USA | 45.95 | −90.27 | CCGG | Flask | NOAA 2006A |
| Lac La Biche, Alberta, Canada | 54.95 | −112.45 | CCGG | Flask | NOAA 2006A |
| Lulin, Taiwan | 23.47 | 120.87 | CCGG | Flask | NOAA 2006A |
| Lampedusa, Italy | 35.52 | 12.62 | CCGG | Flask | NOAA 2006A |
| Mawson Station, Antarctica | −67.62 | 62.87 | CSIRO | Flask | NOAA 2006A |
| Mace Head, Ireland | 53.33 | −9.90 | CCGG, AGAGE | Flask, in situ | NOAA 2006A, SIO-98 |
| Sand Island, Midway Islands | 28.21 | −177.38 | CCGG | Flask | NOAA 2006A |
| Mt. Kenya, Kenya | −0.06 | 37.30 | CCGG | Flask | NOAA 2006A |
| Mauna Loa, Hawaii, USA | 19.54 | −155.58 | CCGG, CATS | Flask, in situ | NOAA 2006A, NOAA 2006A |





GMDD
8, 5367–5418, 2015



**Table 2.** Continued.

| Location | Latitude | Longitude | Network* | Measurement type | Measurement scale |
|---|---|---|---|---|---|
| Macquarie Island, Australia | −54.48 | 158.97 | CSIRO | Flask | NOAA 2006A |
| Gobabeb, Namibia | −23.58 | 15.03 | CCGG | Flask | NOAA 2006A |
| Niwot Ridge, Colorado, USA | 40.05 | −105.55 | CCGG, CATS | Flask, in situ | NOAA 2006A, NOAA 2006A |
| Ochsenkopf, Germany | 50.03 | 11.81 | CCGG | Flask | NOAA 2006A |
| Pallas-Sammaltunturi, Finland | 67.97 | 24.12 | CCGG | Flask | NOAA 2006A |
| Pacific Ocean, Equator | 0.00 | −155.00 | CCGG | Flask | NOAA 2006A |
| Pacific Ocean, 5° N | 5.00 | −151.00 | CCGG | Flask | NOAA 2006A |
| Pacific Ocean, 10° N | 10.00 | −149.00 | CCGG | Flask | NOAA 2006A |
| Pacific Ocean, 15° N | 15.00 | −145.00 | CCGG | Flask | NOAA 2006A |
| Pacific Ocean, 20° N | 20.00 | −141.00 | CCGG | Flask | NOAA 2006A |
| Pacific Ocean, 25° N | 25.00 | −139.00 | CCGG | Flask | NOAA 2006A |
| Pacific Ocean, 30° N | 30.00 | −135.00 | CCGG | Flask | NOAA 2006A |
| Pacific Ocean, 5° S | −5.00 | −159.00 | CCGG | Flask | NOAA 2006A |
| Pacific Ocean, 10° S | −10.00 | −161.00 | CCGG | Flask | NOAA 2006A |
| Pacific Ocean, 15° S | −15.00 | −171.00 | CCGG | Flask | NOAA 2006A |
| Pacific Ocean, 20° S | −20.00 | −174.00 | CCGG | Flask | NOAA 2006A |
| Pacific Ocean, 25° S | −25.00 | −171.00 | CCGG | Flask | NOAA 2006A |
| Pacific Ocean, 30° S | −30.00 | −176.00 | CCGG | Flask | NOAA 2006A |
| Pacific Ocean, 35° S | −35.00 | 180.00 | CCGG | Flask | NOAA 2006A |
| Palmer Station, Antarctica | −64.92 | −64.00 | CCGG | Flask | NOAA 2006A |
| Point Arena, California, USA | 38.96 | −123.74 | CCGG | Flask | NOAA 2006A |
| Ragged Point, Barbados | 13.17 | −59.43 | CCGG, AGAGE | Flask, in situ | NOAA 2006A, SIO-98 |
| Beech Island, South Carolina, USA | 33.41 | −81.83 | CCGG | Flask | NOAA 2006A |
| Mahe Island, Seychelles | −4.68 | 55.53 | CCGG | Flask | NOAA 2006A |
| Sable Island, Nova Scotia, Canada | 43.93 | −60.02 | EC | Flask | NOAA 2006 |
| Southern Great Plains, Oklahoma, USA | 36.61 | −97.49 | CCGG | Flask | NOAA 2006A |
| Shemya Island, Alaska, USA | 52.71 | 174.13 | CCGG | Flask | NOAA 2006A |
| Tutuila, American Samoa | −14.25 | −170.56 | CCGG, CATS | Flask, in situ | NOAA 2006A, NOAA 2006A |
| South Pole, Antarctica | −89.98 | −24.80 | CCGG, CATS | Flask, in situ | NOAA 2006A, NOAA 2006A |
| Schauinsland, Germany | 47.92 | 7.92 | AGAGE | In situ | SIO-98 |
| Sutro Tower, California, USA | 37.76 | −122.45 | CCGG | Flask | NOAA 2006A |
| Summit, Greenland | 72.60 | −38.42 | CCGG, CATS | Flask, in situ | NOAA 2006A, NOAA 2006A |
| Syowa Station, Antarctica | −69.01 | 39.59 | CCGG | Flask | NOAA 2006A |
| Tae-ahn Peninsula, Korea | 36.74 | 126.13 | CCGG | Flask | NOAA 2006A |
| Tierra Del Fuego, Argentina | −54.85 | −68.31 | CCGG | Flask | NOAA 2006A |
| KCMP Tall Tower, Minnesota, USA | 44.68 | −93.07 | | In situ | NOAA 2006A |
| Trinidad Head, California, USA | 41.05 | −124.15 | CCGG, AGAGE | Flask, in situ | NOAA 2006A, SIO-98 |
| Wendover, Utah, USA | 39.90 | −113.72 | CCGG | Flask | NOAA 2006A |
| Ulaan Uul, Mongolia | 44.45 | 111.10 | CCGG | Flask | NOAA 2006A |
| West Branch, Iowa, USA | 41.73 | −91.35 | CCGG | Flask | NOAA 2006A |
| Walnut Grove, California, USA | 38.27 | −121.49 | CCGG | Flask | NOAA 2006A |
| WIS Station, Negev, Desert, Israel | 30.86 | 34.78 | CCGG | Flask | NOAA 2006A |
| Moody, Texas, USA | 31.32 | −97.33 | CCGG | Flask | NOAA 2006A |
| Mt. Waliguan, China | 36.29 | 100.90 | CCGG | Flask | NOAA 2006A |
| Western Pacific Cruise | −30.00 to 30.00 | 136.80 to 168.00 | CCGG | Flask | NOAA 2006A |
| Ny-Ålesund, Svalbard, Norway | 78.91 | 11.89 | CCGG | Flask | NOAA 2006A |

* CCGG: NOAA Carbon Cycle and Greenhouse Gases program; EC: Environment Canada; NIWA: National Institute of Water and Atmospheric research; CATS: NOAA Chromatograph for Atmospheric Trace Species; AGAGE: Advanced Global Atmospheric Gases Experiment.





GMDD
8, 5367–5418, 2015



**Table 3.** Global annual $N_2O$ a posteriori source for all pseudo observation tests.

| Observations | State vector | Initial bias | A posteriori flux ($Tg N yr^{-1}$)[a] | A posteriori sink ($Tg N yr^{-1}$)[b] |
|---|---|---|---|---|
| Surface | Emissions | 0.5, 1.5 | 14.16, 14.25 | – |
| CARIBIC | Emissions | 0.5, 1.5 | 13.82, 14.72 | – |
| HIPPO | Emissions | 0.5, 1.5 | 14.13, 14.32 | – |
| Surface | Emissions + Strat loss frequencies | 0.5, 1.5 | 14.08, 14.78 | 7.69, 25.59 |
| CARIBIC | Emissions + Strat loss frequencies | 0.5, 1.5 | 13.60, 15.66 | 6.73, 20.57 |
| HIPPO | Emissions + Strat loss frequencies | 0.5, 1.5 | 13.99, 14.80 | 7.05, 23.12 |
| Surface | Strat loss frequencies | 0.5, 1.5 | | 11.98, 12.87 |
| CARIBIC | Strat loss frequencies | 0.5, 1.5 | | 10.08, 14.62 |
| HIPPO | Strat loss frequencies | 0.5, 1.5 | | 10.57, 13.91 |
| CARIBIC (no transport error) | Emissions + strat loss frequencies | 0.5 | 14.14 | 9.87 |
| HIPPO (no transport error) | Emissions + strat loss frequencies | 0.5 | 14.09 | 11.26 |
| CARIBIC (no transport error) | Strat loss frequencies | 0.5 | | 11.41 |
| HIPPO (no transport error) | Strat loss frequencies | 0.5 | | 11.60 |
| Surface | Emissions | Seasonal | 13.44 | |
| CARIBIC | Emissions | Seasonal | 13.60 | |
| HIPPO | Emissions | Seasonal | 13.44 | |

[a] True model flux is 14.16 $Tg N yr^{-1}$.
[b] True model stratospheric sink is 12.1 $Tg N yr^{-1}$.





GMDD
8, 5367–5418, 2015



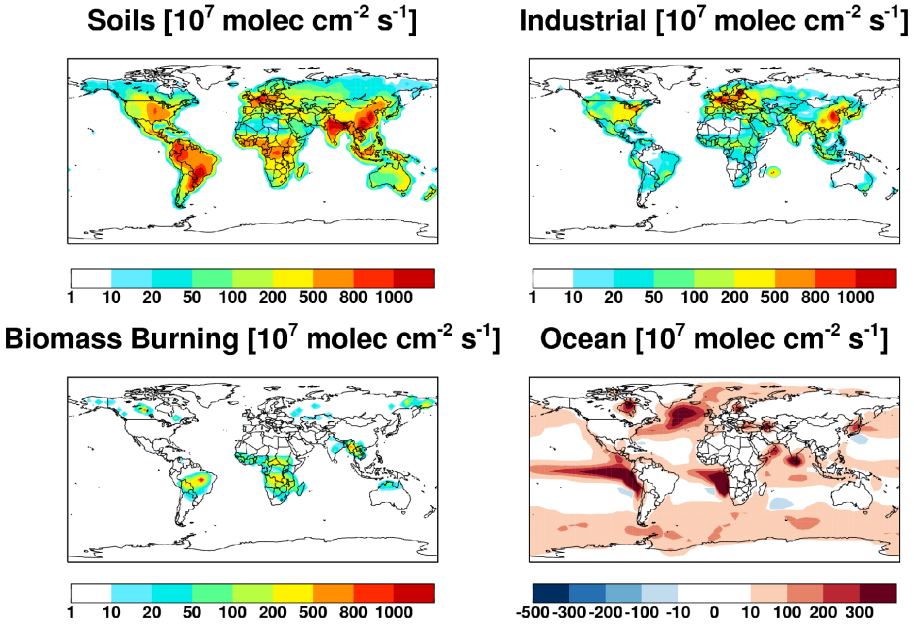


**Figure 1.** Mean annual $N_2O$ fluxes from soils, industrial activities, biomass burning, and ocean exchange in the GEOS-Chem a priori simulation.





GMDD
8, 5367–5418, 2015



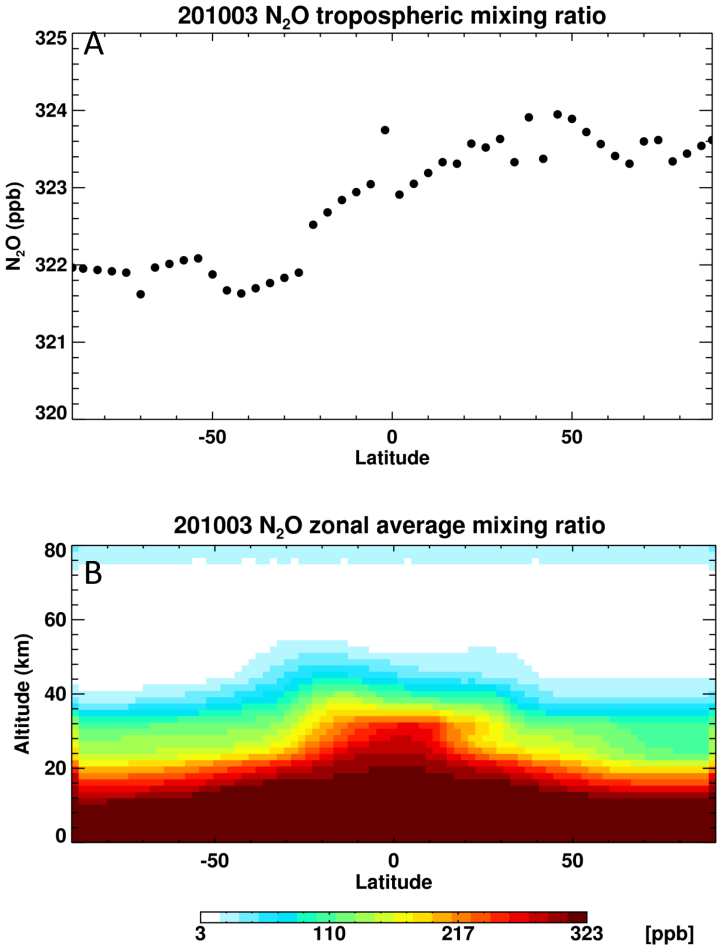


**Figure 2.** Initial model $N_2O$ field for March 2010. Shown are the **(a)** tropospheric $N_2O$ mixing ratios, and **(b)** zonal mixing ratio cross-section.





GMDD
8, 5367–5418, 2015



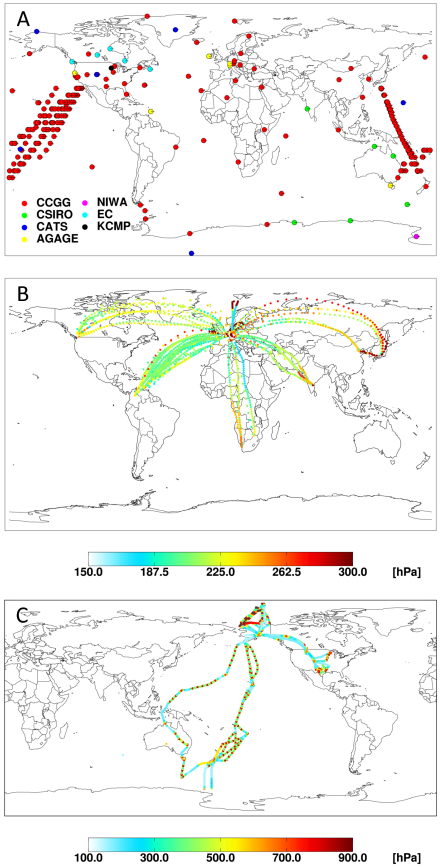


**Figure 3.** Global observing network for atmospheric $N_2O$. Shown are the locations of **(a)** surface observations, **(b)** CARIBIC observations, and **(c)** HIPPO observations. The CARIBIC and HIPPO flights are shaded by the pressure at which the observations were made. Color scales differ between **(b)** and **(c)** to show range of vertical levels sampled in each case.





GMDD
8, 5367–5418, 2015



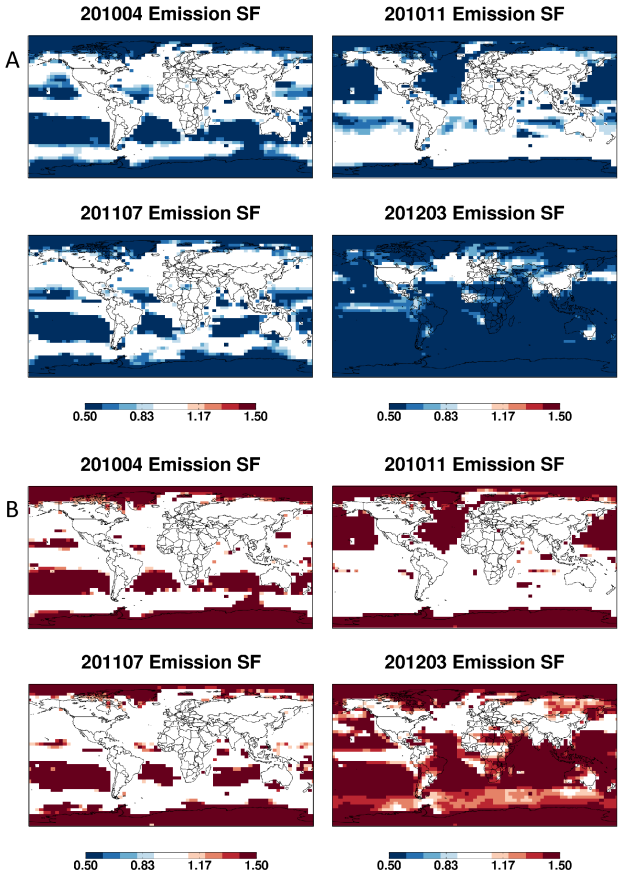


**Figure 4.** Pseudo observation test optimizing $N_2O$ emissions on the basis of surface observations. Shown are a posteriori emission scaling factors using an a priori guess of either **(a)** 0.5 or **(b)** 1.5, where the true value is 1.0. Results are shown for April 2010 (month 1 of the inversion window), November 2010 (month 8), July 2011 (month 16), and March 2012 (month 24).





GMDD
8, 5367–5418, 2015



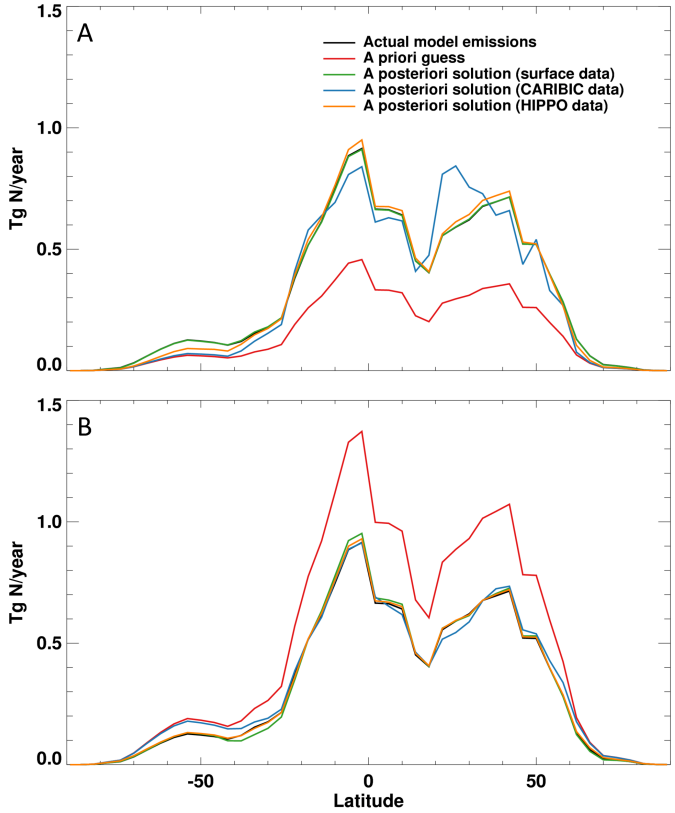


**Figure 5.** Pseudo observation tests optimizing $N_2O$ emissions. Shown are zonally-integrated annual emissions for the first year of the simulation (April 2010–March 2011) starting with an a priori scaling factor of **(a)** 0.5 and **(b)** 1.5, where the true value is 1.0. Actual model emissions are shown in black, model emissions scaled by the a priori guess are shown in red, and a posteriori emissions obtained using surface data, CARIBIC data, and HIPPO data are shown in green, blue, and yellow, respectively.





GMDD
8, 5367–5418, 2015



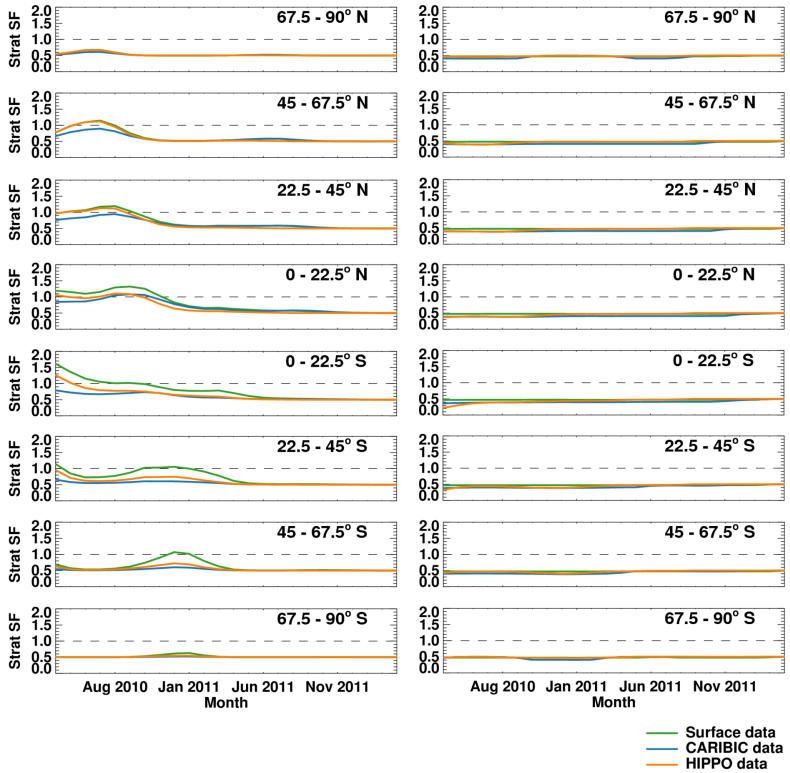


**Figure 6.** Pseudo observation tests optimizing $N_2O$ stratospheric loss frequencies. Shown are a posteriori scaling factors (SF) in each of eight equal latitude bands for pseudo observation tests in which we optimize solely the stratospheric loss frequencies (left panels) or the emissions and stratospheric loss frequencies jointly (right panels). The true model value (1.0) is indicated by the black dashed line; each test started with a priori SF of 0.5 for each latitude band. Results obtained using surface data, CARIBIC data, and HIPPO data are shown in green, blue, and yellow, respectively.





GMDD
8, 5367–5418, 2015



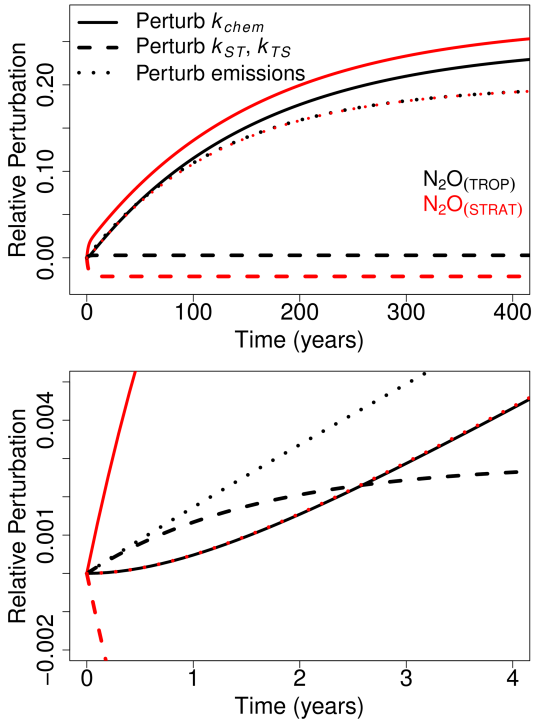


**Figure 7.** Results from a 2-box model illustrating the sensitivity of the tropospheric $N_2O$ burden (and hence source inversions) to the $N_2O$ stratospheric loss rate and to the rate of stratosphere–troposphere exchange. Shown are the relative perturbations to the tropospheric (black lines) and stratospheric (red lines) $N_2O$ burdens resulting from: a 20 % change in the $N_2O$ stratospheric loss frequency ($k_{chem}$, solid lines); a 20 % change in the rate of stratosphere–troposphere exchange ($k_{ST}$ and $k_{TS}$, dashed lines); and a 20 % change in emissions (dotted lines). The top panel shows results over a 400 year timescale, while the bottom panel shows the initial 4 years.





GMDD
8, 5367–5418, 2015



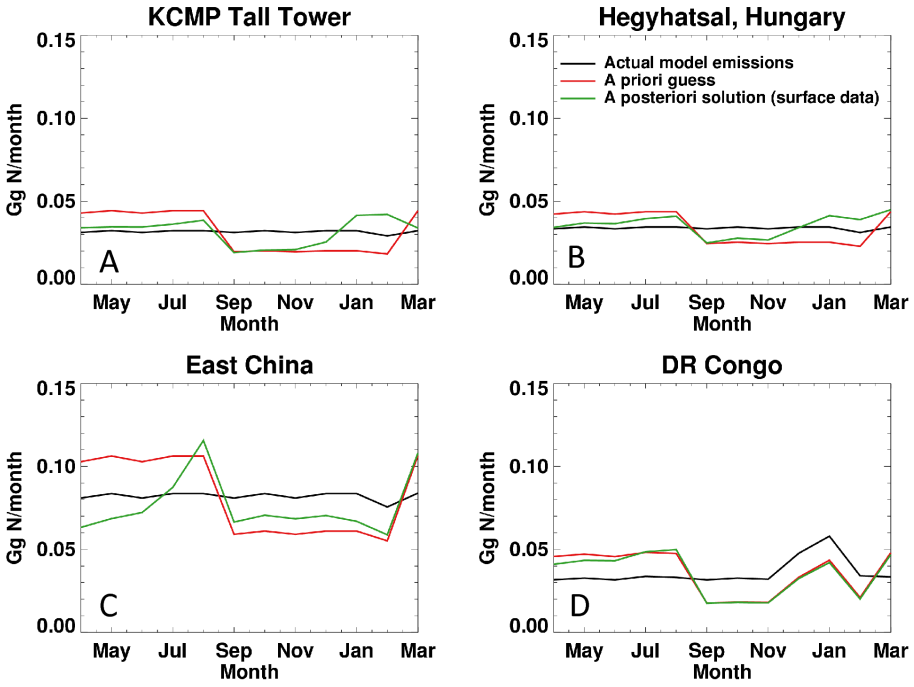


**Figure 8.** Resolving seasonal emission biases. The panels show the results from an OSSE in which a seasonally-dependent a priori emission bias is applied and we test the ability of the inversion to recover the true model fluxes. Results are shown for a site with continuous observations (KCMP Tall Tower), a site with ~ weekly flask observations (Hegyhátsál, Hungary), a site with routine flask measurements ~ 1000 km downwind (East China), and a remote site in the Democratic Republic of Congo (DR Congo). The a priori (red), a posteriori (green) and true model fluxes (black) are plotted for the first year of the simulation (April 2010–March 2011), with the a priori guess for soil emissions biased high in the first half of the inversion period (1.5×; March–August) and biased low in the second half (0.5×; September–February).





GMDD
8, 5367–5418, 2015



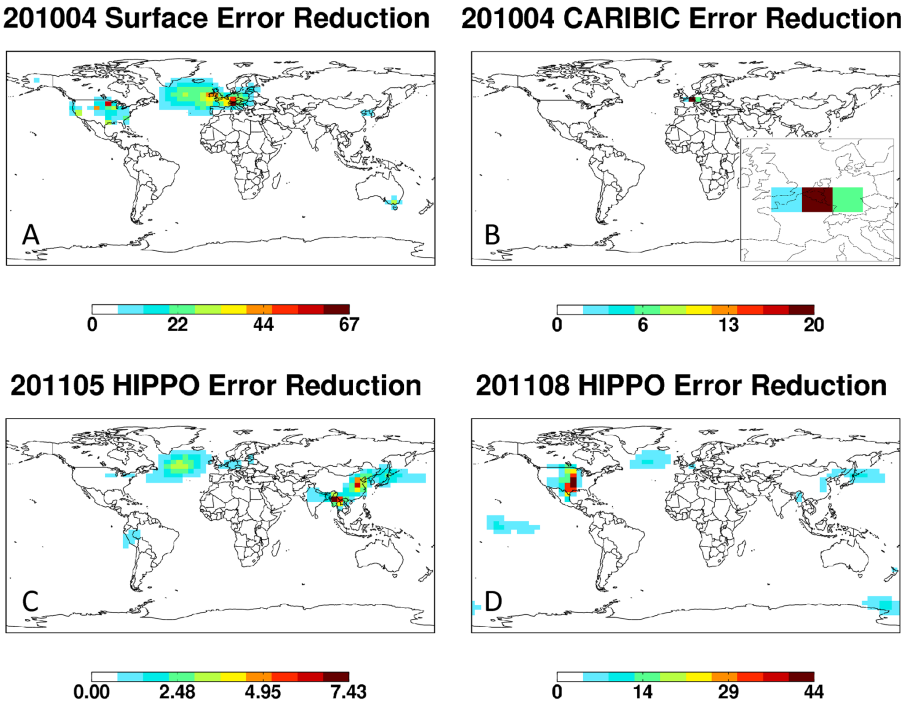


**Figure 9.** Error reduction (%) in $N_2O$ emissions achievable in selected months using surface **(a)**, CARIBIC **(b)**, and HIPPO (**c** and **d**) measurements. An inset shows regional detail for the CARIBIC results. The relative error reduction is calculated based on a stochastic estimate of the inverse Hessian of the cost function for the inversion, and represents the ability of the observing system to remove a random emission error for each given location in the absence of any large-scale source bias.





GMDD
8, 5367–5418, 2015



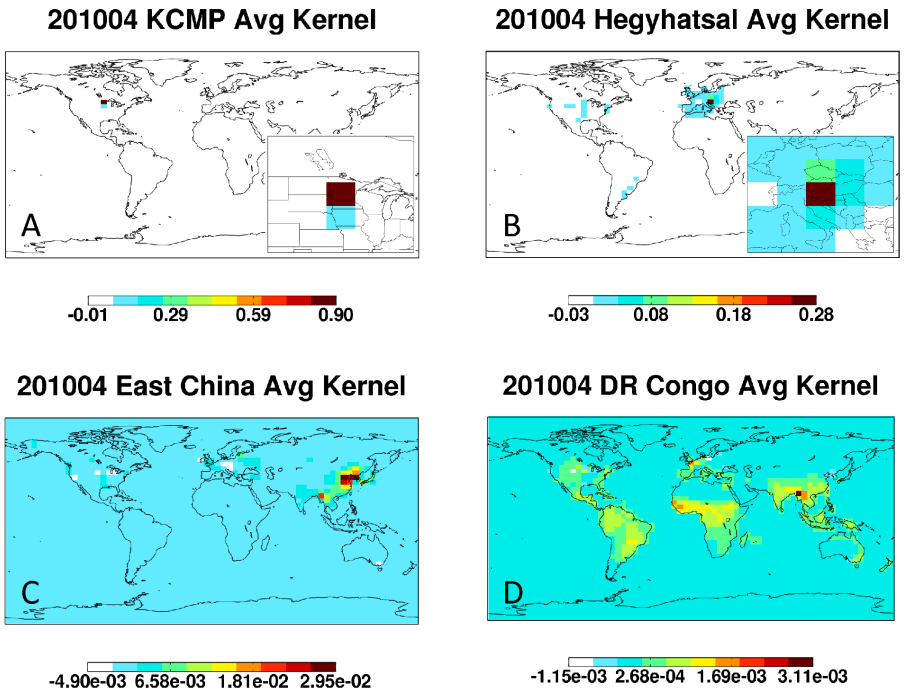


**Figure 10.** Rows of the averaging kernel for the inversion of $N_2O$ emissions based on surface observations. The results indicate how well emissions in a particular location can be resolved from emissions elsewhere, and are shown for four example sites: **(a)** KCMP tall tower, **(b)** Hegyhátsál, Hungary, **(c)** a grid cell in East China, and **(d)** a grid cell in the Democratic Republic of Congo. Insets show regional detail for the first two sites. KCMP is a site with continuous observations, Hegyhátsál is a site with ∼ weekly flask observations, the East China site is a location with flask observations ∼ 1000 km downwind, and the Congo site is a remote location.





GMDD
8, 5367–5418, 2015



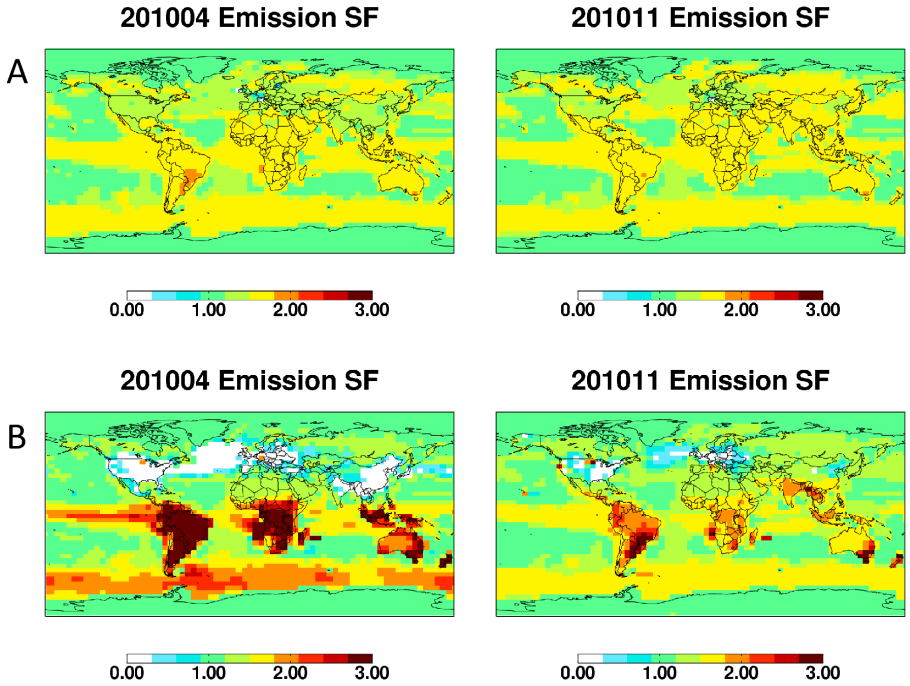


**Figure 11.** Inversion of $N_2O$ emissions based on real surface observations. A posteriori emission scaling factors are shown for two different prior error assumptions: **(a)** 100 % a priori error and horizontal covariance length scales of 500 and 1000 km for land and ocean emissions, respectively; and **(b)** no penalty term in the cost function.





GMDD
8, 5367–5418, 2015



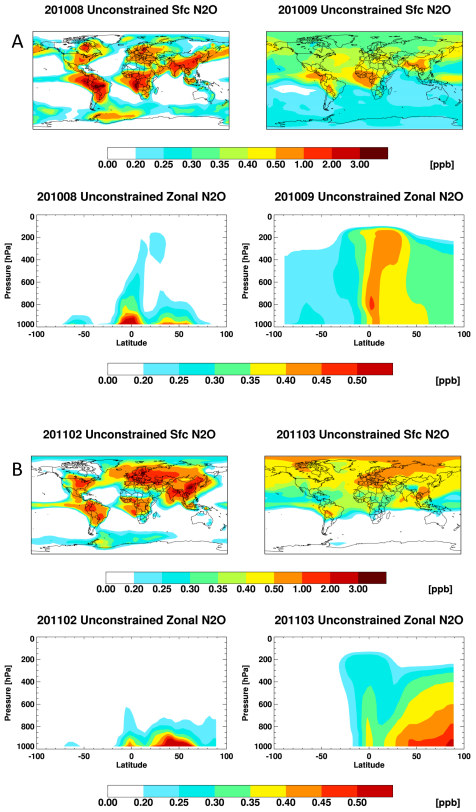


**Figure 12.** Distribution of unconstrained $N_2O$ simulated by GEOS-Chem during the month of emission (August 2010 and February 2011) and the subsequent month. Unconstrained concentrations are calculated by scaling emissions for a particular month by $(1 - \boldsymbol{x})$, where $\boldsymbol{x}$ is the map of emission error reductions achieved using surface observations of $N_2O$. The initial atmospheric burden of $N_2O$ and the emissions in the ensuing months are set to zero in order to highlight the spatial dispersal of unconstrained $N_2O$. Note nonlinear color scales.





GMDD
8, 5367–5418, 2015